Exchange-correlation approximations for reduced-density-matrix-functional theory at finite temperature: Capturing magnetic phase transitions in the homogeneous electron gas

Tim Baldsiefen,[1,2] Attila Cangi,[3,*] F. G. Eich,[4] and E. K. U. Gross[2]

[1]*Institut für Theoretische Physik, Freie Universität Berlin, Arnimallee 14, D-14195 Berlin, Germany*

[2]*Max Planck Institute of Microstructure Physics, Weinberg 2, D-06112 Halle, Germany*

[3]*Center for Computing Research, Sandia National Laboratories, Albuquerque, New Mexico 87185-1321, USA*

[4]*Max Planck Institute for the Structure and Dynamics of Matter, Luruper Chaussee 149, D-22761 Hamburg, Germany*

(Received 14 July 2017; revised manuscript received 10 November 2017; published 18 December 2017)

We derive an intrinsically temperature-dependent approximation to the correlation grand potential for many-electron systems in thermodynamical equilibrium in the context of finite-temperature reduced-density-matrix-functional theory (FT-RDMFT). We demonstrate its accuracy by calculating the magnetic phase diagram of the homogeneous electron gas. We compare it to known limits from highly accurate quantum Monte Carlo calculations as well as to phase diagrams obtained within existing exchange-correlation approximations from density functional theory and zero-temperature RDMFT.

DOI: 10.1103/PhysRevA.96.062508

I. INTRODUCTION

Kohn-Sham density functional theory [1,2] (KS-DFT) has become the most widely applied method in chemistry and materials science for calculating ground-state properties of quantum systems from first principles [3].

However, various interesting physical phenomena at finite temperature pose challenges for its finite-temperature (FT) generalization [4,5]. These include temperature-driven magnetic [6,7] or superconducting [8,9] phase transitions in solids, femtochemistry at surfaces of solids [10], properties of shock compressed noble gases [11,12], the properties of plasmas [13–15], thermal conductivities of inertial confinement fusion capsules [16], and planetary interiors and their formation processes [17–22].

An alternative to KS-DFT is reduced-density-matrix-functional theory (RDMFT). It has several conceptual differences to KS-DFT. Of relevance to our work is that unlike in DFT, both the kinetic energy and the exchange energy are by definition treated exactly because both are expressed explicitly as a functional of the one-body reduced density matrix (1RDM). Only the correlation contribution to the interaction energy needs to be approximated. Therefore, the process of functional construction in RDMFT is distinct from KS-DFT.

The homogeneous electron gas (HEG) is the cornerstone of modern electronic structure theory [23]. An accurate understanding of its properties is intimately related to functional construction in KS-DFT and RDMFT. In DFT, the total energy is a *functional* of the spin densities $\rho_\sigma(\mathbf{r})$, which for the HEG reduces to a *function* of the (spatially constant) spin densities ρ_σ. This function is well known from QMC and many-body calculations. In other words, in DFT the known function $e_{\mathrm{XC}}^{\mathrm{HEG}}(\rho_\sigma)$, the exchange-correlation (XC) energy per particle, serves as input for the functional construction. By construction, in RDMFT, however, the total energy is a functional of the 1RDM which, for the HEG, remains a *functional* (of the momentum-dependent) occupation numbers $n(\mathbf{k})$. This functional is not well known and, therefore, in RDMFT the HEG serves as a test system rather than an exactly known input.

At zero temperature, highly accurate quantum Monte Carlo (QMC) calculations of its XC energy [24,25] form the basis of the local-spin-density approximation (LSDA) [26–28]. Recently, the XC energy of the HEG at finite temperature has been determined using path-integral QMC calculations [29] and parametrized in terms of a temperature-dependent LSDA [30,31].

At zero temperature, RDMFT has been successfully applied to problems that are inherently difficult for KS-DFT. Prominent examples are dissociation energy curves [32–35] and fundamental gaps in molecules, solids [34,36,37], and particularly in Mott insulators [38].

As a central result of this paper we construct a FT-RDMFT correlation functional based on our recent FT generalization of RDMFT [39] and the perturbative methodology introduced therein [39]. As an immediate application, we calculate the magnetic phase diagram of the HEG.

The paper is organized as follows: In Sec. II we briefly review the formalism of FT-RDMFT [39] and introduce the HEG, thereby setting up our notation. We work in atomic units throughout, where $e^2 = \hbar = m_e = 1$ so that lengths are expressed in Bohr radii, and energies in hartree. In Sec. III we summarize our results on the magnetic phase diagram of the HEG. We rationalize the qualitative features of exact phase diagram as a benchmark and assess the predicted phase diagrams within various approximations. We analyze, in particular, the accuracy of the FT-RDMFT correlation approximation (κ-TIE functional) derived in this work. In Sec. IV we calculate the magnetic phase diagram within the FT-RDMFT exchange approximation, i.e., completely neglecting the correlation component of the free energy. We also point out that this is equivalent to FT Hartree-Fock theory. In Sec. V we construct and implement the FT-RDMFT correlation functional (κ-TIE functional) based on the insights gained at zero temperature (see Appendix C). Additionally, we implement the LSDA, random-phase approximation (RPA), and the BOW-TIE functionals in FT-RDMFT and assess the predicted magnetic phase diagrams. Details on the numerical implementation of FT-RDMFT are given in Ref. [40]. Finally,

*acangi@sandia.gov

in Sec. VI we summarize our results and give a perspective on future work. Furthermore, in Appendix A we give an overview of existing zero-temperature RDMFT XC functionals. In Appendix B we discuss planar spin spirals exemplifying a noncollinear spin configuration and extend the magnetic phase diagram within the FT-RDMFT exchange approximation. In Appendix C we identify two properties (reproduction of accurate momentum distributions and spin-channel inseparability) required for an accurate FT-RDMFT XC approximation. We also construct a zero-temperature RDFMT correlation approximation (BOW-TIE functional) satisfying both of these requirements. In Appendix D we demonstrate that RDFMT XC functionals fail in accurately capturing partially polarized spin configurations when spin-channel separability is assumed. Finally, in Appendix E we assess the accuracy of the BOW functional for the two-dimensional (2D) HEG.

II. THEORETICAL FRAMEWORK

A. Overview of FT-RDMFT

Consider a grand-canonical operator

$$\hat{\Omega} = \hat{H} - \mu\hat{N} - \hat{S}/\beta, \tag{1}$$

where $\hat{H}$ denotes the Hamiltonian, $\hat{N}$ the particle number operator, and $\hat{S}$ the entropy operator. In electronic structure theory, $\hat{H}$ usually denotes the electronic Hamiltonian in the Born-Oppenheimer approximation given by $\hat{H} = \hat{T} + \hat{W} + \hat{V}$, where $\hat{T}$ denotes the kinetic energy operator, $\hat{W}$ the Coulombic repulsion operator, and $\hat{V}$ a scalar, external potential. The coupling to the heat and particle baths is achieved via the temperature $1/\beta$ and the chemical potential μ.

Statistical averages such as the grand potential

$$\Omega[\hat{D}] = \mathrm{tr}\{\hat{D}\hat{\Omega}\} \tag{2}$$

are calculated with the statistical density operator (SDO)

$$\hat{D} = \sum_i w_i |\Psi_i\rangle\langle\Psi_i|, \quad w_i \geqslant 0, \quad \sum_i w_i = 1, \tag{3}$$

which is a weighted sum of projection operators on the underlying Hilbert space, where $|\Psi_i\rangle$ and w_i denote the orthonormal N-particle states and their corresponding weights.

The corresponding 1RDM is defined by the SDO and the common fermionic field operators $\hat{\psi}$ as

$$\begin{aligned}\gamma_{\sigma\sigma'}(\mathbf{r},\mathbf{r}') &= \mathrm{tr}\{\hat{D}\hat{\psi}^+_{\sigma'}(\mathbf{r}')\hat{\psi}_\sigma(\mathbf{r})\},\\ &= \sum_i w_i \langle\Psi_i|\hat{\psi}^+_{\sigma'}(\mathbf{r}')\hat{\psi}_\sigma(\mathbf{r})|\Psi_i\rangle.\end{aligned} \tag{4}$$

The 1RDM is Hermitian by construction. Therefore, it is commonly written in its spectral representation, most generally as a matrix in spin space

$$\gamma_{\sigma\sigma'}(\mathbf{r},\mathbf{r}') = \sum_i n_i \Phi_i^\dagger(\mathbf{r}') \otimes \Phi_i(\mathbf{r}) \tag{5}$$

$$= \sum_i n_i \begin{pmatrix} \phi^*_{i1}(\mathbf{r}')\phi_{i1}(\mathbf{r}) & \phi^*_{i2}(\mathbf{r}')\phi_{i1}(\mathbf{r}) \\ \phi^*_{i1}(\mathbf{r}')\phi_{i2}(\mathbf{r}) & \phi^*_{i2}(\mathbf{r}')\phi_{i2}(\mathbf{r}) \end{pmatrix}, \tag{6}$$

where

$$\Phi_i(\mathbf{r}) = \begin{pmatrix} \phi_{i1}(\mathbf{r}) \\ \phi_{i2}(\mathbf{r}) \end{pmatrix} \tag{7}$$

denotes a two-component (Pauli) spinor. This notation is used in Appendix B where we discuss FT-RDMFT for planar spin spiral states in order to illustrate a noncollinear spin configuration.

However, in the remainder of this work we only consider the collinear spin configuration. In this special case, different spin channels can be treated separately in terms of spinors containing only one spin component, where

$$\Phi_{i1}(\mathbf{r}) = \begin{pmatrix} \phi_{i1}(\mathbf{r}) \\ 0 \end{pmatrix}, \quad \Phi_{i2}(\mathbf{r}) = \begin{pmatrix} 0 \\ \phi_{i2}(\mathbf{r}) \end{pmatrix}. \tag{8}$$

This leads to a 1RDM which is diagonal in the spin coordinate

$$\gamma_{\sigma\sigma'}(\mathbf{r},\mathbf{r}') = \delta_{\sigma\sigma'} \sum_i n_{i\sigma} \phi^*_{i\sigma}(\mathbf{r}')\phi_{i\sigma}(\mathbf{r}), \tag{9}$$

where $\{n_{i\sigma}\}$ denote real-valued eigenvalues and $\{\phi_{i\sigma}\}$ the corresponding eigenstates which are called occupation numbers (ONs) and natural orbitals (NOs) [41].

The 1RDM is N representable [42] under the conditions that $\{\phi_i\}$ is a complete set, the fermionic constraint

$$0 \leqslant n_{i\sigma} \leqslant 1, \tag{10}$$

and particle number conservation

$$\sum_i n_{i\sigma} = N_\sigma. \tag{11}$$

The electronic density $\rho(\mathbf{r})$ is determined from the diagonal of the 1RDM, $\rho(\mathbf{r}) = \sum_\sigma \rho_\sigma(\mathbf{r}) = \sum_\sigma \gamma_{\sigma\sigma}(\mathbf{r},\mathbf{r})$.

In our recent work [39] we have established the foundations of FT-RDMFT. We showed that the map between the SDO and the 1RDM at equilibrium is invertible, i.e.,

$$\hat{D}_{\mathrm{eq}} \overset{1-1}{\longleftrightarrow} \mu(\mathbf{r},\mathbf{r}') \overset{1-1}{\longleftrightarrow} \gamma_{\mathrm{eq},\sigma\sigma'}(\mathbf{r},\mathbf{r}'). \tag{12}$$

Furthermore, we showed the existence of a universal functional for the whole set of ensemble-N-representable 1RDMs [39]

$$F[\gamma] = \inf_{\hat{D}\to\gamma} (\mathrm{tr}\{\hat{D}(\hat{T} + \hat{W} - 1/\beta \ln \hat{D})\}) \tag{13}$$

which allows us to write the grand potential as

$$\Omega[\gamma] = F[\gamma] + V[\gamma] - \mu N[\gamma], \tag{14}$$

where $V[\gamma] = \sum_\sigma \int d\mathbf{r}\, d\mathbf{r}' \; [v(\mathbf{r},\mathbf{r}') - \mu\delta(\mathbf{r}-\mathbf{r}')]\gamma_{\sigma\sigma'}(\mathbf{r},\mathbf{r}')$ denotes the statical average over the scalar (and generally nonlocal) external potential $v(\mathbf{r},\mathbf{r}')$ and $N[\gamma] = \sum_\sigma \int d\mathbf{r}\, \gamma_{\sigma\sigma'}(\mathbf{r},\mathbf{r})$ the statistical average over the particle number. Due to the existence of a KS system in FT-RDMFT [39], we express the universal functional in terms of the common KS quantities as

$$F[\gamma] = \Omega_k[\gamma] - \frac{S_S[\gamma]}{\beta} + \Omega_H[\gamma] + \Omega_X[\gamma] + \Omega_C[\gamma], \tag{15}$$

where

$$\Omega_k[\gamma] = \sum_\sigma \int d\mathbf{r} \lim_{\mathbf{r}\to\mathbf{r}'} \left(-\frac{\nabla^2}{2}\right)\gamma_{\sigma\sigma'}(\mathbf{r},\mathbf{r}'), \tag{16}$$

$$S_S[\gamma] = -\sum_{i,\sigma} [n_{i\sigma}\ln(n_{i\sigma}) + (1-n_{i\sigma})\ln(1-n_{i\sigma})], \tag{17}$$

$$\Omega_{\mathrm{H}}[\gamma] = \sum_{\sigma} \frac{1}{2} \int d\mathbf{r}\, d\mathbf{r}'\, w(\mathbf{r}',\mathbf{r}) \gamma_{\sigma\sigma'}(\mathbf{r}',\mathbf{r}') \gamma_{\sigma\sigma'}(\mathbf{r},\mathbf{r}), \quad (18)$$

$$\Omega_{\mathrm{X}}[\gamma] = -\sum_{\sigma} \frac{1}{2} \int d\mathbf{r}\, d\mathbf{r}'\, w(\mathbf{r}',\mathbf{r}) \gamma_{\sigma\sigma'}(\mathbf{r},\mathbf{r}') \gamma_{\sigma\sigma'}(\mathbf{r}',\mathbf{r}) \quad (19)$$

denote the functionals of the kinetic energy, noninteracting entropy, Hartree energy, and exchange energy. The interelectronic interaction is Coulombic and denoted by $w(\mathbf{r},\mathbf{r}') = 1/|\mathbf{r}-\mathbf{r}'|$.

The central goal of this work is to find approximations to the correlation functional $\Omega_{\mathrm{C}}[\gamma]$ at finite temperature. In contrast to DFT, the kinetic energy functional in FT-RDMFT yields the true kinetic energy of the interacting system. Therefore, the correlation functional contains only correlation contributions from the interelectronic interaction and the entropic component. The existence of a KS system allows us to derive an adiabatic connection formula and, consequently, to expand the grand potential functional using methods from FT many-body perturbation theory (MBPT) [39] in order to systematically approximate the correlation functional.

In general, we determine the equilibrium by

$$\Omega_{\mathrm{eq}} = \min_{\gamma \in \Gamma^N} \Omega[\gamma] \quad (20)$$

which is a minimization over the set of all ensemble-N-representable 1RDMs denoted by Γ^N.

Although our perturbative method is explicitly derived assuming a grand-canonical ensemble, we can work within the canonical ensemble [39] such that the domain of minimization is given by the set of all ensemble-N-representable 1RDMs fulfilling the fermionic constraint in Eq. (10) and particle number conservation in Eq. (11) for a fixed particle number N.

Once the correlation functional $\Omega_{\mathrm{C}}[\gamma]$ is approximated, the grand potential $\Omega[\gamma]$ needs to be minimized on the domain of ensemble-N-representable density matrices [43]. In RDMFT, the numerical minimization is usually hampered by imposing auxiliary conditions regarding the fermionic constraint, particle number conservation, and the orthonormality of the NOs. In this work, we employ a self-consistent minimization scheme [40]. It relies on the fact that for every 1RDM in the domain of N-representable 1RDMs, there is a 1RDM from the set of all finite-temperature noninteracting-V-representable 1RDMs arbitrarily close to it [40] and is facilitated by the existence of a KS system in FT-RDFMT [39]. The main idea is then to replace the grand potential $\Omega[\gamma]$ by an effective grand potential $\Omega_{\mathrm{eff}}[\gamma]$ at a different temperature whose minimum will be arbitrarily close to the minimum of $\Omega[\gamma]$ and the requirement that they both have the same functional derivative with respect to γ_k, the 1RDM of iteration cycle k. The minimum of $\Omega_{\mathrm{eff}}[\gamma]$ is then found by a diagonalization of its effective Hamiltonian and an occupation of the new ONs according to the Fermi-Dirac distribution. The resulting 1RDM will then serve as the starting point γ_{k+1} for the subsequent iteration. The variational equations determining γ_k in each iteration step as well as further details on the validation and numerical implementation of this self-consistent minimization scheme are given in Ref. [40].

B. FT-RDMFT for the HEG

The HEG in collinear spin configuration in three dimensions (3D) is an important paradigm for many-electron quantum systems [23,44,45]. Highly accurate QMC calculations [24,29,46,47] provide the basis for parametrizations of its XC energy in terms of density functionals at zero [26–28] and finite temperature [30,31]. The HEG is obtained by considering N electrons in the volume $\mathcal{V}$ and letting both $N \to \infty$ and $\mathcal{V} \to \infty$, while keeping the density $\rho = N/\mathcal{V}$ finite. The density of the HEG is typically defined by the Wigner-Seitz radius

$$r_{\mathrm{S}} = \left(\frac{3}{4\pi\rho}\right)^{1/3}, \quad (21)$$

which is the radius of a sphere with constant density containing one electron. Alternatively, the HEG can be characterized by the Fermi wave vector $k_{\mathrm{F}} = (3\pi^2\rho)^{1/3} = (9\pi/4)^{1/3} r_{\mathrm{S}}^{-1}$, the Fermi energy $\varepsilon_{\mathrm{F}} = k_{\mathrm{F}}^2/2$, and the Fermi temperature $T_{\mathrm{F}} = \varepsilon_{\mathrm{F}}/k_B$. Introducing the polarization

$$\xi = \frac{\rho_\uparrow - \rho_\downarrow}{\rho_\uparrow + \rho_\downarrow} \quad (22)$$

in terms of the spin-resolved densities $\rho_\uparrow$ and $\rho_\downarrow$, where $\rho_\sigma = \rho(1 \pm \xi)$, allows us to express the Fermi wave vector, the Fermi energy, and Fermi temperature of each spin channel as

$$k_{\sigma\mathrm{F}} = k_{\mathrm{F}}(1 \pm \xi)^{1/3}, \quad (23)$$

$$\varepsilon_{\sigma\mathrm{F}} = \varepsilon_{\mathrm{F}}(1 \pm \xi)^{2/3}, \quad (24)$$

$$T_{\sigma\mathrm{F}} = T_{\mathrm{F}}(1 \pm \xi)^{2/3}. \quad (25)$$

The 1RDM of the HEG is given by

$$\gamma_{\sigma\sigma'}(\mathbf{r}-\mathbf{r}') = \delta_{\sigma\sigma'} \int \frac{d^3k}{(2\pi)^3}\, n_\sigma(\mathbf{k})\, e^{i\mathbf{k}\cdot(\mathbf{r}-\mathbf{r}')}, \quad (26)$$

where the NOs are planes waves, the ONs $n_\sigma(\mathbf{k})$ denote the momentum distribution of spin channel σ, and the polarization in FT-RDMFT is defined through the ONs by

$$\xi = \frac{N_\uparrow - N_\downarrow}{N_\uparrow + N_\downarrow} \quad (27)$$

with

$$N_\sigma = (2\pi)^{-3} \int d^3k\, n_\sigma(\mathbf{k}) \quad (28)$$

with the spin-dependent ONs of Eq. (9).

Considering the positive charge background to retain charge neutrality, the universal functional of the HEG simplifies to

$$F[\gamma] = \Omega_k[\gamma] + \Omega_{\mathrm{X}}[\gamma] + \Omega_{\mathrm{C}}[\gamma] - \frac{S_{\mathrm{S}}[\gamma]}{\beta} \quad (29)$$

and also coincides with its free-energy functional. The equilibrium is determined by

$$F_{\mathrm{eq}} = \min_{\gamma} F[\gamma]. \quad (30)$$

The individual energy components simplify to

$$\Omega_k[\gamma] = \frac{1}{\rho}\sum_\sigma \int \frac{d^3k}{(2\pi)^3} n_\sigma(\mathbf{k})\frac{k^2}{2}, \tag{31}$$

$$\Omega_x[\gamma] = -\frac{1}{2\rho}\sum_\sigma \int \frac{dk_1^3}{(2\pi)^3}\int \frac{dk_2^3}{(2\pi)^3} \times n_\sigma(\mathbf{k}) n_\sigma(\mathbf{k}')\frac{4\pi}{(\mathbf{k}-\mathbf{k}')^2}, \tag{32}$$

$$S_S[\gamma] = -\frac{1}{\rho}\sum_\sigma \int \frac{d^3k}{(2\pi)^3}(n_\sigma(\mathbf{k})\ln[n_\sigma(\mathbf{k})] + [1-n_\sigma(\mathbf{k})]\ln[1-n_\sigma(\mathbf{k})]). \tag{33}$$

In the numerical treatment, we assume the ONs to be constant in small volumes $\mathcal{V}_i$ around the k points $\mathbf{k}_i$. Equations (31)–(33) then transform into sums yielding

$$\Omega_k[\{n_{i\sigma}\}] = \sum_{i,\sigma} n_{i\sigma} t_i, \tag{34}$$

$$\Omega_x[\{n_{i\sigma}\}] = -\frac{1}{2}\sum_{i,j,\sigma} n_{i\sigma} n_{j\sigma} K_{i,j}, \tag{35}$$

$$S_S[\{n_{i\sigma}\}] = -\sum_{i,\sigma}(n_{i\sigma}\ln(n_{i\sigma}) + (1-n_{i\sigma})\ln(1-n_{i\sigma}))\omega_i, \tag{36}$$

where

$$t_i = \frac{1}{\rho}\int_{\mathcal{V}_i}\frac{d^3k}{(2\pi)^3}\frac{k^2}{2}, \tag{37}$$

$$K_{i,j} = \frac{1}{\rho}\int_{\mathcal{V}_i}\frac{dk_1^3}{(2\pi)^3}\int_{\mathcal{V}_j}\frac{dk_2^3}{(2\pi)^3}\frac{4\pi}{(\mathbf{k}-\mathbf{k}')^2}, \tag{38}$$

$$\omega_i = \frac{1}{\rho}\int_{\mathcal{V}_i}\frac{d^3k}{(2\pi)^3}. \tag{39}$$

III. SUMMARY OF RESULTS: MAGNETIC PHASE TRANSITIONS IN THE HEG

A. Magnetic phase diagram of the HEG

The magnetic phase diagram is our benchmark to assess the accuracy of FT-RDMFT correlation approximations developed in this paper. The phase diagram is constructed by calculating and comparing free energies of different phases. We distinguish between the fully polarized collinear states which we call *ferromagnetic* (FM) phase, unpolarized states which we call *paramagnetic* (PM) phase, and *partially polarized* (PP) phase.

Although the exact phase diagram of the HEG is not known, we can rationalize its qualitative behavior. At zero temperature and a sufficiently large r_S, the equilibrium configuration is the FM phase. With decreasing r_S we expect a continuous phase transition from the FM to the PM phase. QMC calculations predict this phase transition to occur within a critical Wigner-Seitz radius of $r_c \approx 50\ldots75$ [24,46]. At finite temperature, the characteristic energy of the system is given by the Fermi energy ε_F and the corresponding Fermi temperature is T_F. With increasing temperature, the entropic contribution becomes increasingly dominant. Therefore, we expect a phase transition from the FM phase, over an intermediate PP phase, eventually to the PM phase.

Note that we assume a collinear spin configuration. In Appendix B we discuss planar spin spirals exemplifying a more general, noncollinear spin configuration.

B. Magnetic phase diagram of the HEG within the Stoner model

Consider a HEG with collinear spin configuration in 3D within the Stoner model [46,48,49]. This amounts to replacing the Coulomb interaction by a contact interaction

$$w^S(\mathbf{r},\mathbf{r}') \propto r_S^2(1-\delta_{\sigma_1\sigma_2})\delta(\mathbf{r}-\mathbf{r}') \tag{40}$$

and including this as a first-order perturbation on top of the noninteracting HEG. Then, we obtain the free-energy functional within the Stoner model

$$F[\gamma] = \Omega_k[\gamma] + \Omega_W^S[\gamma] - \frac{S_S[\gamma]}{\beta}, \tag{41}$$

where the interaction grand potential is simply given in terms of the polarization ξ by

$$\Omega_W^S[\gamma] = \frac{g(1-\xi^2)}{r_S}. \tag{42}$$

The interaction strength is denoted by g. Its value is determined by requiring the Stoner model to reproduce the zero-temperature phase transition between FM and PM phases to occur at a critical Wigner-Seitz radius $r_c \approx 60$. This yields an interaction strength $g \approx 0.0102$.

C. Summary of magnetic phase diagrams

We summarize the main results of this paper in Fig. 1. It illustrates the behavior of the magnetic phase diagram of the HEG within various approximations. In the following, we compare these approximate phase diagrams with each other and with our expectations for the exact phase diagram. In particular, we expect the critical temperature T_c on the order of the Fermi temperature T_F.

The phase diagram of the Stoner model is shown in Fig. 1(a). By construction, the zero-temperature phase transition between the FM and PM phases occurs within the correct Wigner-Seitz radius $r_c \approx 60$. Furthermore, it predicts a finite-temperature transition at $r_c^T \approx 80$ with a critical temperature $T_c \approx 49$ K. However, the critical temperature T_c of the finite-temperature transition at r_c^T is underestimated compared to the Fermi temperature $T_F \approx 90$ K. Although the Stoner model is capable of predicting quite a reasonable phase diagram, it is nevertheless only a heuristic model.

The phase diagram of the FT-RDMFT exchange-only calculation (which is identical to a FT-Hartree-Fock calculation) is shown in Fig. 1(b). It significantly underestimates the zero-temperature phase transition between the FM and PM phases predicting $r_c \approx 5.45$ [23]. The finite-temperature transition is predicted at $r_c^T \approx 7.1$ with a corresponding critical temperature of $T_c \approx 10\,500$ K. This approximation is qualitatively reasonable by predicting the critical temperature of the finite-temperature transition as $T_C \approx T_F$. However, it predicts an unphysical, instantaneous phase transition from the FM to PM phase (depicted by a dashed red line).

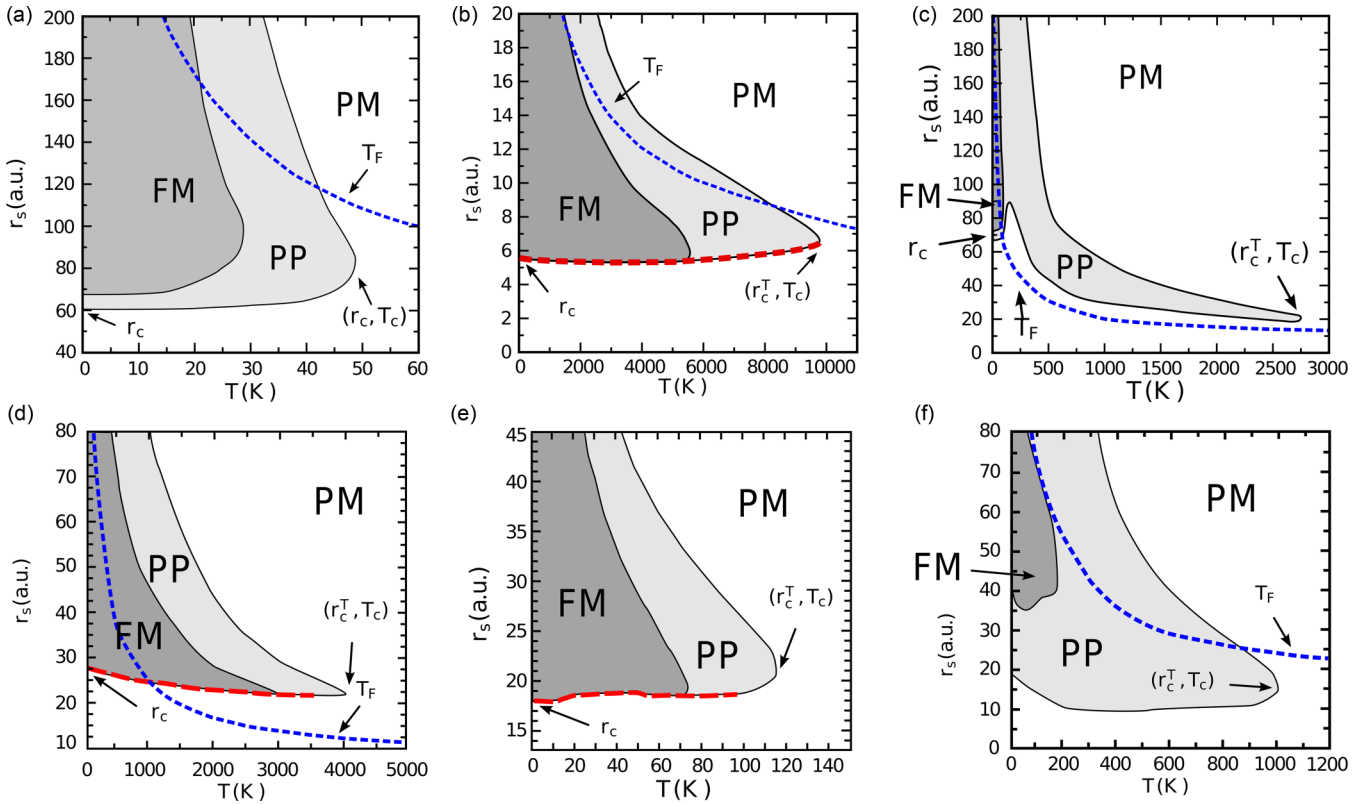

FIG. 1. Magnetic phase diagrams of the HEG in collinear spin configuration within various approximations: the Stoner model in (a), the FT-RDMFT exchange functional in (b), the FT-RDMFT LSDA functional in (c), the BOW-TIE correlation functional in (d), the FT-RPA correlation functional in (e), and the κ-TIE correlation functional in (f). The dashed blue line depicts the Fermi temperature T_F. The dashed red line depicts an unphysical, instantaneous phase transition. Note that the κ-TIE correlation functional in (f) correctly predicts a continuous, second-order phase transition from the FM to the PM phase.

In Fig. 1(c) we show the phase diagram when the LSDA in the well-known PW parametrization [28] is applied within FT-RDMFT. By construction, the zero-temperature transition occurs at the correct Wigner-Seitz radius $r_c \approx 70$. However, the LSDA correlation functional given in Eq. (45) does not take into the momentum distribution of the occupation numbers and is therefore expected to be inaccurate at finite temperature. For $20 < r_S < 80$ and temperatures greater than T_F, the phase diagram is irregular. At finite temperature it predicts a phase transition from the PM to the PP phase and eventually another transition back to the PM phase at $r_c^T \approx 20$ overestimating the critical temperature $T_c \approx 2750$ K compared to the Fermi temperature $T_F \approx 1250$ K.

The phase diagram resulting from the BOW-TIE functional [derived in Eq. (C8)] is shown in Fig. 1(d). The zero-temperature transition is underestimated predicting $r_c \approx 28$. It predicts the finite-temperature transition at $r_c^T \approx 21$ overestimating the critical temperature $T_c \approx 4000$ K compared to the Fermi temperature $T_F \approx 1100$ K. Furthermore, it also predicts an unphysical, instantaneous phase transition from the FM to the PM phase.

In Fig. 1(e) we illustrate the phase diagram when the FT-RPA density functional is used within FT-RDMFT. The zero-temperature transition is underestimated predicting $r_c \approx 18$. The finite-temperature transition is predicted at $r_c^T \approx 21$ with a critical temperature $T_C \approx 115$ K which is much smaller than the Fermi temperature $T_F \approx 1300$ K. Furthermore, it also predicts an unphysical, instantaneous phase transition from the FM to the PM phase.

Finally, in Fig. 1(f) we illustrate the phase diagram resulting from the intrinsically temperature-dependent FT-RDMFT correlation functional (κ-TIE functional) derived in Eq. (69). The zero-temperature transition is at $r_c \approx 19$. The finite-temperature phase transition is at $r_c^T \approx 15$ with a critical temperature $T_c \approx 1000$ K somewhat smaller than the Fermi temperature $T_F \approx 2200$ K. Nevertheless, this approximation yields a physically reasonable phase diagram with a physically correct second-order phase transition between the FM and the PM phases and a qualitatively improved momentum distribution compared to other RDMFT functionals.

IV. EXCHANGE IN FT-RDMFT

Consider Eq. (29) without the correlation contribution. This yields the free-energy functional

$$F[\{n_{i\sigma}\}] = \Omega_k[\{n_{i\sigma}\}] + \Omega_x[\{n_{i\sigma}\}] - 1/\beta S_S[\{n_{i\sigma}\}], \quad (43)$$

where the individual energy components are defined in Eqs. (34)–(36). Note that this functional is identical to the Hartree-Fock functional and that minimizing Eq. (43) is equivalent to solving the FT Hartree-Fock equations [50,51]. Note that we only discuss the collinear spin configuration here. An example of a noncollinear spin configuration is given in Appendix B where we investigate the magnetic phase diagram

of the planar spin spiral configuration within the exchange level.

We begin by calculating the magnetic phase diagram of the HEG as a function of the temperature and the Wigner-Seitz radius r_S. The result is shown in Fig. 1(b). We find an unphysical, instantaneous phase transition between the PM and the FM phases with increasing r_S. We can understand this transition by considering how the individual energy components of the free energy depend on r_S. The kinetic contribution favoring a PM phase is proportional to r_S^{-2}, the exchange contribution favoring a FM phase is proportional to r_S^{-1}, and the entropy favoring a PM phase has no explicit dependence on r_S. First consider the zero-temperature phase transition. The kinetic contribution is dominant for small r_S leading to a PM phase. With increasing r_S, the effect of the exchange contribution becomes increasingly important, overcoming the kinetic contribution at some critical Wigner-Seitz radius $r_c = 5.45$ [23] where a magnetic phase transition from the PM to the FM phase occurs. In order to understand the phase transition at finite temperature, we also need to take into account the entropic contribution. With increasing r_S, it eventually dominates over kinetic and exchange contributions. Hence, the PM phase becomes favorable for increasing r_S at any finite temperature. At a critical Wigner-Seitz radius $r_c^T = 7.1$ and a critical temperature $T_c \approx 10\,500$ K the PM phase dominates. Furthermore, the phase diagram illustrates how the FM phase vanishes faster with increasing temperature. This behavior can be attributed to the temperature prefactor of the entropic contribution.

Note that the instantaneous phase transition between the PM and FM phases is unphysical and persists at finite temperature. It only occurs due to the incapability of the exchange approximation. In the real system we expect a second-order phase transition which has been predicted by highly accurate QMC calculations so far only at zero temperature [46].

Nevertheless, the exchange RDMFT functional yields a qualitatively correct prediction of the critical temperature $T_C \approx T_F$. This suggests that the noninteracting entropy functional accurately captures a large fraction of the total interacting entropy.

V. CORRELATION IN FT-RDMFT

We begin by pointing out a conceptual difference between DFT and RDMFT. In DFT, constructing the LSDA requires parametrizing the correlation energy of the HEG as a function of r_S for a constant density ρ. On the other hand, constructing an analogous local reduced-density-matrix approximation (LRDMA) requires parametrizing the HEG for all possible density matrices $\gamma_{\sigma\sigma'}(\mathbf{r}-\mathbf{r}')$ that are compatible with translational invariance, i.e., for all possible momentum distributions $n(\mathbf{k})$. Hence, in RDMFT the HEG correlation energy per volume becomes $\varepsilon_C^{\mathrm{HEG}}[\gamma_{\sigma\sigma'}(\mathbf{k},\mathbf{R})]$, a *functional* of $n(\mathbf{k})$ rather than just of ρ. Assuming that this functional is accessible, the LRDMA of RDMFT is defined as

$$E_C^{\mathrm{LRDMA}}[\gamma_{\sigma\sigma'}(\mathbf{r},\mathbf{r}')] = \int d^3R\, \varepsilon_C^{\mathrm{HEG}}[\gamma_{\sigma\sigma'}(\mathbf{k},\mathbf{R})], \tag{44}$$

where E_c^{LRDMA} denotes an approximate correlation energy of a nonuniform system and $\gamma_{\sigma\sigma'}(\mathbf{k},\mathbf{R}) = \int d^3s\, \gamma_{\sigma\sigma'}(\mathbf{R}+\mathbf{s}/2, \mathbf{R}-\mathbf{s}/2)\exp(i\mathbf{k}\cdot\mathbf{s})$ the Wigner transform of the 1RDM. This procedure is similar to defining the LDA in superconducting DFT [52,53]. While there are many LSDA constructions conceivable that correctly reduce to the homogeneous limit, Eq. (44) is the only definition that correctly reproduces the correlation energy of a *weakly inhomogeneous* electron gas [53].

Despite some attempts [54,55], construction of a reliable LRDMA remains an important task for the future. Its extension to spin-dependent configurations and finite temperature is conceptually straightforward. However, calculating the temperature-dependent $\varepsilon_c^{\mathrm{HEG}}[n(\mathbf{k}),T]$ through path-integral QMC and similar techniques [25] is complicated by the fermionic sign problem [56]. Therefore, we can only revert to constructing approximate RDMFT correlation functionals based on the HEG.

In this work, we derive an intrinsically temperature-dependent approximation to the correlation functional in FT-RDMFT (κ-TIE functional). Our construction is based on two properties required for an accurate FT-RDMFT correlation functional: it needs to (i) accurately capture the momentum distribution, i.e., simultaneously give the correct occupation of high-momentum states and the depletion of low-momentum states; (ii) be spin-channel inseparable to be capable of accurately describing both spin-polarized and spin-unpolarized configurations. Neither of these two requirements is fulfilled by existing RDFMT functionals. The importance of the momentum distribution within the LSDA for the excited-state exchange functional has recently been analyzed [57]. In Appendix C we lay the groundwork for the finite-temperature case by deriving the BOW and BOW-TIE zero-temperature RDMFT correlation functionals which simultaneously satisfy both (i) and (ii).

We begin by implementing existing XC approximations (LSDA, BOW-TIE, FT-RPA) in FT-RDMFT and calculating the magnetic phase diagram of the HEG within these approximations. Then, we derive the κ-TIE functional as an intrinsically temperature-dependent correlation functional and assess its accuracy.

A. LSDA correlation

We implement the LSDA within the PW parametrization [28] as follows. Using the result in Eq. (C2), we remove the kinetic correlation energy at zero temperature yielding the free-energy functional

$$F \overset{T\to 0}{=} \Omega_k[n(\mathbf{k})] + \Omega_x[n(\mathbf{k})] + W_C^{\mathrm{PW}}(\rho). \tag{45}$$

It yields exactly the parametrized QMC results because the momentum distribution is a step function. At finite temperature we reinclude the kinetic correlation to restore the accuracy of the LSDA.

The resulting phase diagram shown in Fig. 1(c). By construction, the zero-temperature transition occurs at the correct Wigner-Seitz radius $r_c \approx 70$. However, in the range $20 < r_S < 80$ and temperatures greater than T_F, the phase diagram is irregular. With increasing temperature, it predicts a phase transition from the PM to the PP phase and eventually another transition back to the PM phase at $r_c^T \approx 20$. It yields a the critical temperature $T_c \approx 2750$ K which is larger than

the Fermi temperature $T_F \approx 1250$ K. We attribute the vast PP phase for temperatures above T_F to the uncorrelated nature of the 1RDM when density functionals are used within RDMFT. Hence, the noninteracting entropy functional underestimates the real entropy.

B. BOW-TIE correlation functional

We implement the BOW-TIE functional given in Eq. (C8) in FT-RDMFT with the parameters listed in Table V in FT-RDMFT. The resulting phase diagram is shown in Fig. 1(d). The zero-temperature transition is at $r_c \approx 28$. The finite-temperature transition occurs at $r_c^T \approx 21$. The critical temperature $T_c \approx 4000$ K is much larger than the Fermi temperature $T_F \approx 1100$ K. Furthermore, the BOW-TIE functional also predicts an unphysical, instantaneous phase transition from the FM to the PM phase.

C. FT-RPA correlation

We implement the FT-RPA correlation grand potential in FT-RDMFT, but resorting to the momentum distribution $n(\mathbf{k})$ from DFT according to the noninteracting Fermi-Dirac distribution. In FT-RPA, the correlation component of the grand potential is defined as

$$\Omega_C^{\mathrm{RPA}} = \frac{1}{2\beta}\int \frac{d^3q}{(2\pi)^3}\sum_{a=-\infty}^{\infty}\{\ln[1 - W(\mathbf{q})\chi(\mathbf{q},\nu_a)] + W(\mathbf{q})\chi(\mathbf{q},\nu_a)\}, \tag{46}$$

where $\nu_a = 2\pi a/\beta$ denote the Matsubara frequencies, $W(\mathbf{q}) = 4\pi/q^2$ the Fourier transform of the Coulomb interaction, and

$$\chi(\mathbf{q},\nu_a) = \chi_\uparrow(\mathbf{q},\nu_a) + \chi_\downarrow(\mathbf{q},\nu_a) \tag{47}$$

with

$$\chi_\sigma(\mathbf{q},\nu_a) = -\int \frac{d^3k}{(2\pi)^3}\frac{n_\sigma(\mathbf{k}+\mathbf{q}) - n_\sigma(\mathbf{k})}{\mathbf{i}\nu_a - [\varepsilon_\sigma(\mathbf{k}+\mathbf{q}) - \varepsilon_\sigma(\mathbf{k})]} \tag{48}$$

denotes the polarization propagator. FT-RPA calculations have already been performed for the unpolarized HEG [58,59]. However, here we perform calculations for arbitrary polarization and temperature. The resulting phase diagram is shown in Fig. 1(e). The zero-temperature transition is underestimated by predicting $r_c \approx 18$ due to the 1RDM again being uncorrelated in the zero-temperature limit. The finite-temperature transition occurs at $r_c^T \approx 21$ with a critical temperature $T_C \approx 115$ K which is much smaller than the Fermi temperature $T_F \approx 1300$ K. Furthermore, it also predicts an unphysical, instantaneous phase transition from the FM to the PM phase.

D. κ-TIE correlation functional

None of the functionals implemented and investigated so far (LSDA, BOW-TIE, and FT-RPA) are true FT-RDMFT correlation functionals. They either have no explicit temperature dependence or are just functionals of the density and not the 1RDM.

In the following, we derive the κ-TIE correlation functional as the central result of this work. It is a FT-RDMFT functional because it depends on the full momentum distribution and the temperature explicitly. Our approach is to use the methodology of FT-MBPT introduced in Ref. [39]. We split the derivation into three steps. First, we point out the conceptual difficulty of variational collapse when FT-MBPT is used to construct FT-RDMFT correlation functionals. We then propose a solution by approximating the polarization propagator directly as a functional of the momentum distribution. Finally, we add the *transchannel interaction energy* (TIE) to make our functional spin inseparable.

1. Variational collapse

Consider the free energy in Eq. (29) where the correlation grand potential is given within RPA defined in Eqs. (46)–(48). The free-energy components Ω_k, V, S_S, and Ω_x only depend on the momentum distribution directly, whereas Ω_C^{RPA} also depends explicitly on the KS energies. This poses a problem in FT-RDMFT as we show in the following.

Through the one-to-one correspondence between the ground-state density ρ and the KS potential v_S, the correlation grand potential Ω_C^{RPA} is an implicit functional of the KS energies $\varepsilon(\mathbf{k})$. We can roughly determine the dependence of Ω_C^{RPA} on these by parametrizing them as $\varepsilon(m;\mathbf{k}) = k^2/(2m)$, where we choose the effective mass m as a variational parameter. We then find

$$n(t,m;\mathbf{k}) = \frac{1}{1 + e^{\frac{k^2}{mt} - \alpha(mt)}} = n(mt,1;\mathbf{k}), \tag{49}$$

where we introduced the reduced temperature $t = T/T_F$ and the fugacity $\alpha = \beta\mu$. Decreasing the variational parameter m leads to a smoother momentum distribution. With this parametrized momentum distribution we investigate the qualitative behavior of the components in the FT-RDMFT energy functional under a change in $n(\mathbf{k})$. From Eq. (49) we infer that all functionals just depending on the momentum distribution show the same simple dependence on m:

$$\Omega_k(t,m) = \Omega_k(mt,1), \tag{50}$$

$$V(t,m) = V(mt,1), \tag{51}$$

$$N(t,m) = N(mt,1), \tag{52}$$

$$S_S(t,m) = S_S(mt,1), \tag{53}$$

$$\Omega_x(t,m) = \Omega_x(mt,1), \tag{54}$$

$$F(t,m) = E_k(mt,1) + V(mt,1) - 1/\beta S_S(mt,1) + \Omega_x(mt,1). \tag{55}$$

Note that $F(t,m) \neq F(mt,1)$ because of the temperature prefactor of S_S. On the other hand, the polarization propagator in RPA exhibits a different behavior because it depends on $\varepsilon(m;\mathbf{k})$ explicitly:

$$\chi_\sigma(t,m;q,\nu_a) = m\chi_\sigma(mt,1;q,\nu_a). \tag{56}$$

Now, consider the limit $t \to 0$ while keeping the product mt and therefore the momentum distribution fixed, i.e., $t \to 0$, $m \propto 1/t$. All contributions up to first order in the

interaction stay invariant under this transformation. The free energy changes because of the prefactor $1/\beta$ in front of S_S. However, under the assumption that we started from a finite entropy, this free-energy change remains finite. On the other hand, the polarization and, hence, Ω_C^{RPA} diverge because of the prefactor m.

Therefore, a straightforward inclusion of higher-order diagrams from FT-MBPT will most likely lead to ill-behaved FT-RDMFT correlation functionals, yielding wrong energies and momentum distributions. Note that this does not disprove the validity of the perturbation expansion of $\Omega[\gamma]$ [39]. It only shows that utilizing a subset of diagrams in a variational scheme might result in a variational collapse. This is due to the total freedom in choice for $\varepsilon(\mathbf{k})$ by the inclusion of nonlocal potentials, a fact also recently pointed out in the context of GW [60].

2. *Approximating the polarization propagator directly as a functional of the momentum distribution*

In order to avoid a possible variational collapse, we propose to model the perturbative expressions from FT-MBPT using only approximations to the momentum distribution.

We propose a frequency-independent model for the polarization propagator $\chi(\mathbf{q})$, in line with the COHSEX approximation [61]. Using

$$\frac{\partial n(\mathbf{k})}{\partial \varepsilon(\mathbf{k})} = -\beta n(\mathbf{k})[1 - n(\mathbf{k})], \tag{57}$$

the kernel of $\chi(\mathbf{q},0)$ to second order in the limit $\mathbf{q} \to 0$ is given by

$$\frac{n(\mathbf{k}+\mathbf{q}) - n(\mathbf{k})}{\varepsilon(\mathbf{k}+\mathbf{q}) - \varepsilon(\mathbf{k})} = \frac{\partial n(\mathbf{k})}{\partial \varepsilon(\mathbf{k})}\left(1 + \frac{\beta\left[n(\mathbf{k}) - \frac{1}{2}\right]\sum_{i,j} q_i q_j \frac{\partial \varepsilon(\mathbf{k})}{\partial k_i}\frac{\partial \varepsilon(\mathbf{k})}{\partial k_j}}{\sum_i q_i \frac{\partial \varepsilon(\mathbf{k})}{\partial k_i}}\right). \tag{58}$$

The second term in Eq. (58) vanishes in the integration over $\mathbf{k}$, assuming point symmetry around the origin for the ONs and eigenenergies, i.e., $n_\sigma(\mathbf{k}) = n_\sigma(-\mathbf{k})$ and $\varepsilon(\mathbf{k}) = \varepsilon(-\mathbf{k})$. Hence, the polarization propagator in the limit $\mathbf{q} \to 0$ reduces to

$$\chi_\sigma(\mathbf{q}) \xrightarrow{q\to 0} -\beta \int \frac{d^3k}{(2\pi)^3} n_\sigma(\mathbf{k})[1 - n_\sigma(\mathbf{k})] + O(q^2). \tag{59}$$

Next, we need to determine the momentum dependence of the polarization propagator for large $\mathbf{q}$. Neglecting the frequency dependence and using the spatial isotropy of the interaction, we rewrite the RPA correlation grand potential in Eq. (46) as

$$\tilde{\Omega}_C^{RPA} = \frac{1}{\beta(2\pi)^2} \int dq\, q^2 \{\ln[1 - W(\mathbf{q})\chi(\mathbf{q})] + W(\mathbf{q})\chi(\mathbf{q})\}. \tag{60}$$

We define β/q^2 as a measure that determines the magnitude of $W(\mathbf{q})\chi(\mathbf{q})$. Based on this, we split the integral in Eq. (60) in two parts:

$$\tilde{\Omega}_C^{RPA} \approx \tilde{\Omega}_C^{RPA,0} + \tilde{\Omega}_C^{RPA,\infty}. \tag{61}$$

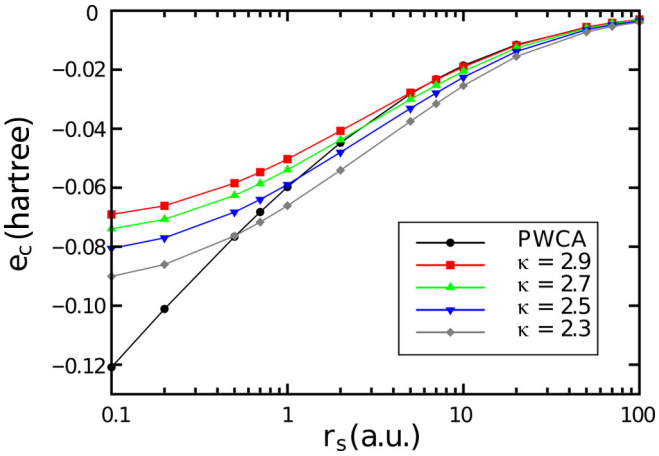

FIG. 2. Comparison of the exact QMC correlation energy of the 3D HEG in the PW parametrization [28] (black curve) with the predictions of the κ functional for various values of κ.

When $q < \tilde{q} = \sqrt{\beta}$, the value of $W(\mathbf{q})\chi(\mathbf{q})$ is large which allows us to neglect the logarithm yielding

$$\tilde{\Omega}_C^{RPA,0} = \frac{1}{\beta(2\pi)^2} \int_0^{\tilde{q}} dq\, q^2 (W(\mathbf{q})\chi(\mathbf{q})) \tag{62}$$

$$= \frac{4\pi}{\beta(2\pi)^2} \int_0^{\sqrt{\beta}} dq (\chi(\mathbf{q})). \tag{63}$$

When $q > \tilde{q}$, $W(\mathbf{q})\chi(\mathbf{q})$ is small. Expanding the logarithm for small argument then yields

$$\tilde{\Omega}_C^{RPA,\infty} = -\frac{1}{\beta(2\pi)^2} \int_{\sqrt{\beta}}^{\infty} dq\, q^2 \frac{(W(\mathbf{q})\chi(\mathbf{q}))^2}{2}. \tag{64}$$

We deduce from Eq. (63) that $\tilde{\Omega}_C^{RPA,0}$ diverges in the limit $T \to 0$, i.e., $\beta \to \infty$, unless $\chi(\mathbf{q})$ behaves like

$$\chi(\mathbf{q}) \xrightarrow{q\to\infty} \propto q^\kappa, \quad \kappa \leqslant -2. \tag{65}$$

Based on these exact limits of the polarization propagator we propose the following κ functional in the separated form of Eq. (61) as

$$\Omega_C^\kappa[n(\mathbf{k})](\mathbf{q}) = \frac{1}{\beta\pi} \int_0^{\sqrt{\beta}} dq\, \chi^\kappa[n(\mathbf{k})](\mathbf{q}) - \frac{1}{2\beta(2\pi)^2} \times \int_{\sqrt{\beta}}^{\infty} dq\, q^2 \{W(\mathbf{q})\, \chi^\kappa[n(\mathbf{k})](\mathbf{q})\}^2, \tag{66}$$

where

$$\chi_\sigma^\kappa[n_\sigma(\mathbf{k})](\mathbf{q}) = -\frac{\beta\left(\rho_\sigma - \langle\rho_\sigma^2\rangle\right)}{1 + (q/k_F)^\kappa} \tag{67}$$

with

$$\langle\rho_\sigma^2\rangle = \int \frac{d^3k}{(2\pi)^3} n_\sigma^2(\mathbf{k}). \tag{68}$$

The prefactor of β ensures that Ω_C^{RPA} remains finite in the limit $\beta \to \infty$.

We calculate the correlation energy using the κ functional in the zero-temperature limit for various values of κ. The results in Fig. 2 demonstrate its reasonable accuracy. Additionally,

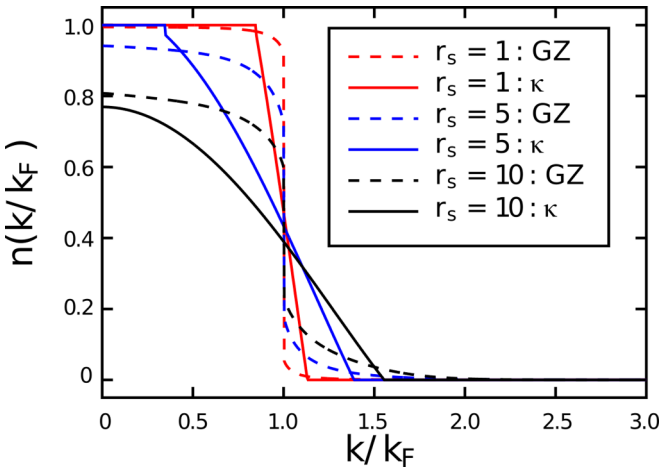

FIG. 3. Momentum distributions of the 3D HEG for $r_S = 1$, 5, and 10 obtained from the parametrization by Gori-Giorgi and Ziesche [55] and from the κ functional for $\kappa = 2.9$.

in Fig. 3 we show that the κ functional (here with the choice $\kappa = 2.9$) yields accurate momentum distribution as we required in our earlier discussion.

Furthermore, the κ functional is spin-channel inseparable when we include a polarization dependence $\kappa(\xi)$. The parameters that optimally reproduce the correlation energy of the HEG in the range $1 < r_S < 100$ are listed in Table I.

3. *Including the transchannel interaction energy*

Like the BOW functional, also the κ functional fails to predict the zero-temperature phase transition. We therefore propose a modification similar to the BOW-TIE functional in Eq. (C8) to recover a correction prediction of the FM phase at low densities:

$$\chi_\sigma^{\kappa\text{-TIE}}[n(\mathbf{k})](\mathbf{q}) = -\chi_\sigma^{\kappa}[n(\mathbf{k})](\mathbf{q}) - \frac{c\,\beta}{1+q^2/k_F^2} \times \int \frac{d^3k}{(2\pi)^3} n_\uparrow(\mathbf{k}) n_\downarrow(\mathbf{k})[1 - n_\uparrow(\mathbf{k}) n_\downarrow(\mathbf{k})]. \tag{69}$$

The optimal set of parameters which yield accurate correlation energies for arbitrary polarization over the whole range of densities is listed in Table II.

Finally, in Fig. 1(f) we illustrate the resulting phase diagram of the explicitly temperature-dependent κ-TIE functional given in Eq. (69). The zero-temperature transition is at $r_c \approx 19$. The finite-temperature phase transition occurs at $r_c^T \approx 15$ with a critical temperature $T_c \approx 1000$ K which is smaller than the Fermi temperature $T_F \approx 2200$ K. Nevertheless, this approximation yields a physically reasonable phase diagram with a physically correct second-order phase transition between the FM and the PM phase and a qualitatively improved momentum distribution compared to other RDMFT XC functionals.

TABLE I. Optimal polarization dependent parameter $\kappa(\xi)$ of the κ functional for the 3D HEG in the range $1 < r_S < 100$.

ξ	0.0	0.1	0.2	0.3	0.4	0.5
$\kappa(\xi)$	2.9	2.9	2.9	3.0	3.0	3.0
ξ	0.6	0.7	0.8	0.9	1.0	
$\kappa(\xi)$	3.1	3.1	3.1	3.2	3.2	

TABLE II. Optimal parameters of the κ-TIE functional defined in Eq. (69).

	κ	c
κ-TIE	3.2	0.24

VI. CONCLUSIONS

In this work we have derived an explicitly temperature-dependent approximation to the correlation energy for use in FT-RDMFT. We first focused on the zero-temperature case, where we identified two properties an accurate functional should recover: its ability to yield an accurate momentum distribution and to be spin-channel inseparable. We derive a zero-temperature correlation functional (BOW-TIE functional) satisfying both of these requirements and demonstrated its superior accuracy to existing zero-temperature RDMFT XC functionals. With the insight gained at zero temperature, we construct the κ-TIE correlation functional for FT-RDMFT. As an immediate application, we calculate the magnetic phase diagram of the HEG. Additionally, we calculated the corresponding phase diagrams within the exchange approximation, the LSDA, the RPA, and the BOW-TIE approximation. Our assessment of the resulting phase diagrams demonstrates the ability of the κ-TIE functional in capturing the expected qualitative features of the exact phase diagram. In particular, it yields a physically correct second-order phase transition between the FM and the PM phase and a qualitatively improved momentum distribution compared to other RDMFT XC functionals. The caveat of the κ-TIE functional is that it underestimates the zero-temperature phase transition between the FM and PM phases. An accurate prediction of this phase transition is complicated by the small energy differences between the distinct phases over a wide range of densities. However, in real solids, phase transitions occur at much higher densities with a stronger dependence of energy differences on the density. With their accurate qualitative predictions over a wide range of densities, we expect both the BOW-TIE and κ-TIE functionals to be suitable approximations for capturing correlation effects and predicting phase transitions for a wide range of real solids.

ACKNOWLEDGMENTS

A.C. was supported by Sandia's Laboratory Directed Research and Development Project No. 200202. Sandia National Laboratories is a multimission laboratory managed and operated by National Technology and Engineering Solutions of Sandia, LLC, a wholly owned subsidiary of Honeywell International, Inc., for the US Department of Energy's National Nuclear Security Administration under Contract No. DE-NA-0003525.

APPENDIX A: BRIEF OVERVIEW OF ZERO-TEMPERATURE RDMFT XC FUNCTIONALS

In this Appendix we give a brief overview of existing zero-temperature RDMFT XC functionals. Most RDMFT XC functionals approximate the correlation energy by a modification of the exchange functional given in Eq. (19). The general form of an RDFMT XC functional can be written as

$$E_{\mathrm{XC}}[\gamma] = E_x[\gamma] + E_c[\gamma] \tag{A1}$$

$$= -\frac{1}{2}\sum_{ij\sigma} f(n_{i\sigma},n_{j\sigma}) \int d\mathbf{r}\, d\mathbf{r}'\, w(\mathbf{r},\mathbf{r}')\phi^*_{i\sigma}(\mathbf{r}') \times \phi_{i\sigma}(\mathbf{r})\phi^*_{j\sigma}(\mathbf{r})\phi_{j\sigma}(\mathbf{r}'). \tag{A2}$$

The various approximations mainly differ by their choice of $f(n_{i\sigma},n_{j\sigma})$. Choosing $f^x(n_{i\sigma},n_{j\sigma}) = n_{i\sigma}n_{j\sigma}$ reproduces the exchange-only functional, neglecting correlation completely.

The first approximation to $f(n_{i\sigma},n_{j\sigma})$ was the Müller functional [62,63] $f^M(n_{i\sigma},n_{j\sigma}) = \sqrt{n_{i\sigma}n_{j\sigma}}$. It is able to correctly describe the dissociation limit of several small dimers of open-shell atoms, but it overestimates the correlation energy quite considerably.

Inspired by its simple functional form, the BBC1, BBC2, and BBC3 functionals [32] were developed. They differ in their treatment of occupied and unoccupied orbitals obtained from the Hartree-Fock solution. In addition, BBC2 and BBC3 effectively mix parts of the exchange and Müller functionals.

A very similar approach is behind the PNOF0 and PNOF functionals [64], where parts of the self-interaction are removed (PNOF0) and particle-hole symmetry is incorporated (PNOF). These more elaborate functionals (BBC1/2/3 and PNOF/0) yield good dissociation energies as well as correlation energies.

Whereas the previous functionals are mainly derived from physical arguments, the ML and ML-SIC functionals [65] are based on two-parameter Padé approximants for $f(n_{i\sigma},n_{j\sigma})$. The parameters in these functionals are optimized to minimize the deviation of correlation energies of molecules in the standardized G2 and G2-1 data sets. ML and ML-SIC (which includes a self-interaction correction) achieve an unprecedented precision, reaching the accuracy of second-order Møller-Plesset perturbation theory for correlation energies. A more comprehensive overview of their performance is given in Ref. [66].

Another, rather empirical, functional is the power functional [38] $f^\alpha(n_{i\sigma},n_{j\sigma};\alpha) = (n_{i\sigma}n_{j\sigma})^\alpha$ which is obtained by changing the exponent α in the Müller functional. Since the Müller functional underestimates the correlation energy, varying α between 0.5 and 1 improves the accuracy [34], leading to an accurate dissociation energy curve of the hydrogen molecule [67]. Also note that only the power functional among these functionals is spin-channel inseparable.

APPENDIX B: FT-RDMFT EXCHANGE FOR PLANAR SPIN SPIRALS

In this Appendix we consider planar spin spirals (PSS) as an example of a more general spin configuration in the HEG at finite temperature.

It was shown that spin-density waves in the HEG at zero temperature have an energy lower than the PM state within the Hartree-Fock approximation [68]. Here, we investigate this with respect to increasing temperature, closely following a recent analysis of spin-density waves within zero-temperature RDMFT [69].

The NOs describing spin-density waves also yield a spin-channel separable 1RDM given by

$$\phi_{1\mathbf{k}}(\mathbf{r}) = \begin{pmatrix} \cos\left(\frac{\Theta_k}{2}\right)e^{-i\mathbf{q}\cdot\mathbf{r}/2} \\ \sin\left(\frac{\Theta_k}{2}\right)e^{i\mathbf{q}\cdot\mathbf{r}/2} \end{pmatrix} \frac{e^{i\mathbf{k}\cdot\mathbf{r}}}{\sqrt{\mathcal{V}}}, \tag{B1}$$

$$\phi_{2\mathbf{k}}(\mathbf{r}) = \begin{pmatrix} -\sin\left(\frac{\Theta_k}{2}\right)e^{-i\mathbf{q}\cdot\mathbf{r}/2} \\ \cos\left(\frac{\Theta_k}{2}\right)e^{i\mathbf{q}\cdot\mathbf{r}/2} \end{pmatrix} \frac{e^{i\mathbf{k}\cdot\mathbf{r}}}{\sqrt{\mathcal{V}}}, \tag{B2}$$

where $\mathbf{q}$ denotes the wave vector, Θ_k the azimuthal angle of the spin spirals, and $\mathcal{V}$ the volume of the space under consideration. The spin channels do not exhibit spin-up or -down characteristics but describe spin spirals. In the collinear basis, the 1RDM becomes

$$\gamma_{\uparrow\uparrow}(\mathbf{r},\mathbf{r}';\mathbf{q},\Theta_k) = \int \frac{d^3k}{(2\pi)^3}\left[n_{1\mathbf{k}}\cos^2\frac{\Theta_k}{2} + n_{2\mathbf{k}}\sin^2\frac{\Theta_k}{2}\right] \times e^{i(\mathbf{k}-\mathbf{q}/2)\cdot(\mathbf{r}-\mathbf{r}')}, \tag{B3}$$

$$\gamma_{\uparrow\downarrow}(\mathbf{r},\mathbf{r}';\mathbf{q},\Theta_k) = \int \frac{d^3k}{(2\pi)^3}\frac{n_{1\mathbf{k}}-n_{2\mathbf{k}}}{2} \times \sin\Theta_k\, e^{i\mathbf{k}\cdot(\mathbf{r}-\mathbf{r}')}\, e^{i\mathbf{q}\cdot(\mathbf{r}+\mathbf{r}')/2}, \tag{B4}$$

$$\gamma_{\downarrow\uparrow}(\mathbf{r},\mathbf{r}';\mathbf{q},\Theta_k) = \int \frac{d^3k}{(2\pi)^3}\frac{n_{1\mathbf{k}}-n_{2\mathbf{k}}}{2} \times \sin\Theta_k\, e^{i\mathbf{k}\cdot(\mathbf{r}-\mathbf{r}')}\, e^{-i\mathbf{q}\cdot(\mathbf{r}+\mathbf{r}')/2}, \tag{B5}$$

$$\gamma_{\downarrow\downarrow}(\mathbf{r},\mathbf{r}';\mathbf{q},\Theta_k) = \int \frac{d^3k}{(2\pi)^3}\left[n_{1\mathbf{k}}\sin^2\frac{\Theta_k}{2} + n_{2\mathbf{k}}\cos^2\frac{\Theta_k}{2}\right] \times e^{i(\mathbf{k}+\mathbf{q}/2)\cdot(\mathbf{r}-\mathbf{r}')}. \tag{B6}$$

Here, we only consider planar spin-density waves, i.e., spin-density waves for which the magnetization of the HEG in z direction vanishes ($B = 0$). As argued in Refs. [70] and [69], this planar configuration has a lower energy than a conical spin-density wave with nonvanishing z component. Furthermore, we only consider spin-density waves with $\mathbf{q}$ parallel to the z axis. We call these PSS. The symmetry of the system suggests the use of cylindrical coordinates such that $\mathbf{k} = (k_z,k_\rho,\phi)$. The free-energy functional then reads as

$$F[\{n_{ib},\Theta_i\}] = \sum_{i,b} n_{ib}t_i + \frac{q^2}{8} - q\sum_i (n_{i1}-n_{i2})\cos(\Theta_i)Q_i - \frac{1}{2}\sum_{i,j,b}(n_{ib}n_{bj})\cos^2\left(\frac{\Theta_i-\Theta_j}{2}\right)K_{ij} - \sum_{i,j,b}(n_{ib}n_{jb})\sin^2\left(\frac{\Theta_i-\Theta_j}{2}\right)K_{ij} + 1/\beta\sum_{ib}(n_{ib}\ln(n_{ib})+(1-n_{ib})\ln(1-n_{ib}))\omega_i, \tag{B7}$$

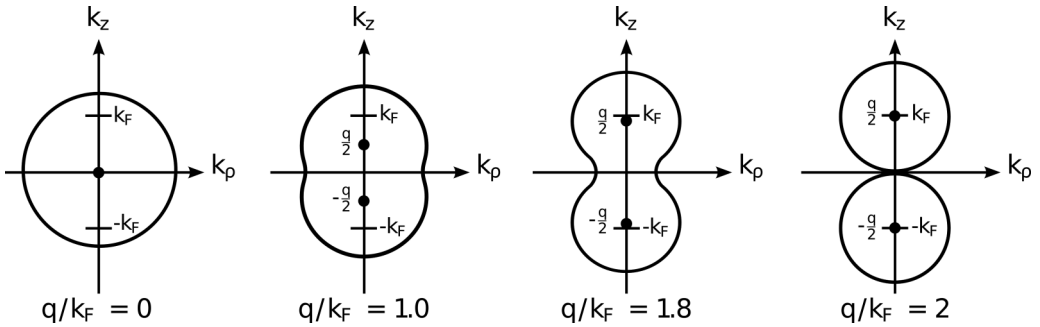

FIG. 4. Sketch of the Fermi surface as a function of $\mathbf{q}$ in a fully polarized PSS state.

where

$$Q_i = \frac{1}{2\rho}\int_{\mathcal{V}_i}\frac{d^3k}{(2\pi)^3}k_z \tag{B8}$$

with t_i, K_{ij}, and w_i given in Eqs. (37)–(39). We also introduce an index b in order to distinguish spin-density waves from collinear spin states. The magnetization of the HEG with spin-density waves as NOs is given by

$$\mathbf{m}(\mathbf{r}) = -\begin{pmatrix} A\cos(\mathbf{q}\cdot\mathbf{r}) \\ A\sin(\mathbf{q}\cdot\mathbf{r}) \\ B \end{pmatrix} \tag{B9}$$

with the two amplitudes

$$A = \frac{1}{2}\int\frac{d^3k}{(2\pi)^3}(n_{\mathbf{k}1}-n_{\mathbf{k}2})\sin(\Theta_{\mathbf{k}}) \tag{B10}$$

(B11)

and

$$B = \frac{1}{2}\int\frac{d^3k}{(2\pi)^3}(n_{\mathbf{k}1}-n_{\mathbf{k}2})\cos(\Theta_{\mathbf{k}}). \tag{B12}$$

We meet the requirement of vanishing z component by imposing these constraints on the ONs and NOs:

$$n_{(k_\rho,-k_z)b} = n_{(k_\rho,k_z)b}, \tag{B13}$$

$$\Theta_{(k_\rho,\pm|k_z|)} = \frac{\pi}{2}(1\mp a_{(k_\rho,|k_z|)}). \tag{B14}$$

We can now minimize the free-energy functional with respect to the ONs and orbital angles. In order to compare the free energy of PSS with the collinear spin configuration at finite temperature, we define the PSS polarization as

$$\xi^{\mathrm{PSS}} = \frac{N_1-N_2}{N_1+N_2}, \tag{B15}$$

where $N_1 = \sum_i n_{i1}$ and $N_2 = \sum_i n_{i2}$. Setting $\mathbf{q}=0$ and $a_{k_\rho|k_z|}=1$, the PSS-NOs become

$$\phi_{(k_\rho,\pm|k_z|)1}(\mathbf{r}) = \frac{1}{\sqrt{2}}\begin{pmatrix}1\pm1\\1\mp1\end{pmatrix}\frac{e^{i\mathbf{k}\cdot\mathbf{r}}}{\sqrt{\Omega}} \tag{B16}$$

and

$$\phi_{(k_\rho,\pm|k_z|)2}(\mathbf{r}) = \frac{1}{\sqrt{2}}\begin{pmatrix}-(1\mp1)\\1\pm1\end{pmatrix}\frac{e^{i\mathbf{k}\cdot\mathbf{r}}}{\sqrt{\Omega}}. \tag{B17}$$

For this set of NOs, the PSS-unpolarized state $\xi^{\mathrm{PSS}}=0$ corresponds to the PM phase and the PSS-polarized state $\xi^{\mathrm{PSS}}=1$ describes the FM phase.

In order to illustrate the effect of increasing q, we sketch the q dependence of the Fermi surface in a fully polarized noninteracting system in Fig. 4. For $q=0$, the ONs describe a Fermi sphere of radius $2^{1/3}k_{\mathrm{F}}$ around $k=0$. With increasing q, the Fermi sphere divides symmetrically along the z direction. We can derive this behavior from the first three terms in Eq. (B7) and the symmetry relations given in Eqs. (B13) and (B14). If q supercedes $2k_{\mathrm{F}}$, then there are two distinct Fermi spheres with radius k_{F}, centered at $k=-q/2$ and $q/2$, respectively. Including temperature effects leads to a washed-out momentum distribution around the Fermi surface.

By varying q alone, we can compare the free energies of the FM collinear configuration ($q=0$, $\xi^{\mathrm{PSS}}=1$), the fully polarized PSS configuration with finite q and the PM collinear configuration ($q\to\infty$, $\xi^{\mathrm{PSS}}=1$). The q dependence of the free energy as well as its kinetic, exchange, and entropic components at various temperatures are shown in Fig. 5. The entropy shows a monotonically increasing, almost linear, dependence until the two Fermi spheres are completely separated (at $q\approx 2k_{\mathrm{F}}$). This increase of entropy in turn leads to an increase of the optimal q vector (the q for which the free energy is minimal). This situation is depicted in Fig. 6 for

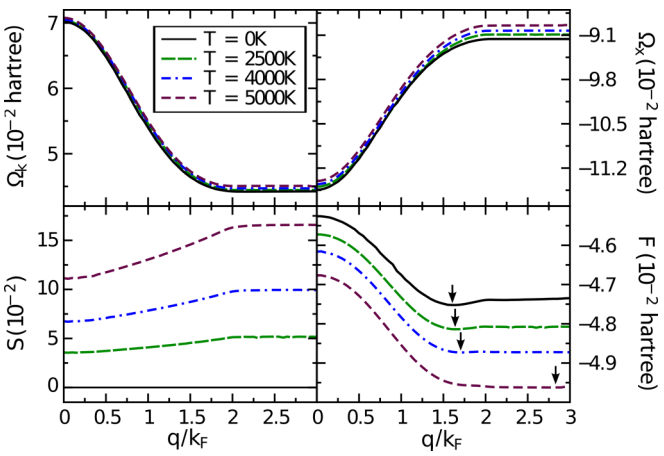

FIG. 5. Clockwise from top left: kinetic energy, exchange energy, free energy, and entropy at $r_{\mathrm{S}}=5$ and ($T_{\mathrm{F}}=23\,300$ K) as a function of the PSS $\mathbf{q}$ vector. The minimal free energies are denoted by the arrows.

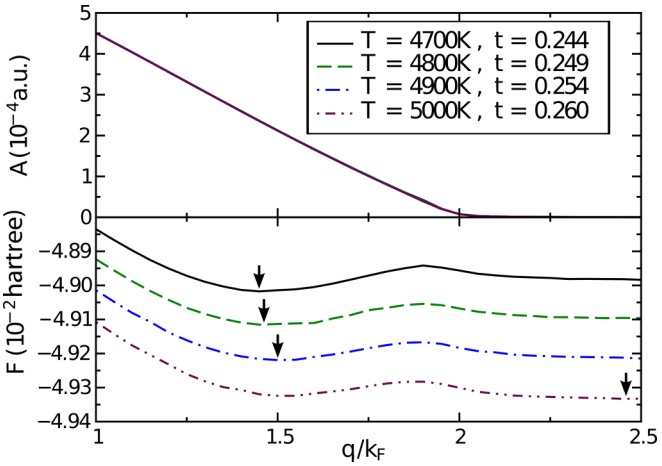

FIG. 6. Amplitude A and free energy F at fixed $r_S = 5.5$ as a function of q for various temperatures $T = 4700$, 4800, 4900, 5000 K. The amplitudes change only slightly with increasing temperature, but the optimal q increases (arrows) discontinuously, letting the optimal amplitude A_{opt} vanish. This denotes an instantaneous phase transition in the PSS phase.

$r_S = 5.50$, where we show the free energy and the amplitude of a PSS state as a function of q for several temperatures. Below some critical temperature T_c^{PSS}, the free energy has a minimum for finite q. Above some T_c^{PSS}, q_{min} instantaneously jumps to a value bigger than $2k_F$, letting the amplitude of the PSS vanish. This jump marks an instantaneous phase transition of the PSS phase, where the amplitude of the optimal PSS is approaching zero instantaneously. In his work on spin-density waves, Overhauser [68] conjectured that the optimal amplitude of the spin-density wave continuously approaches zero with increasing temperature, giving rise to a continuous phase transition. Our results disprove the validity of this conjecture for PSS states.

We show the dependence of the optimal PSS amplitude for several r_S as a function of T in Fig. 7. For small q

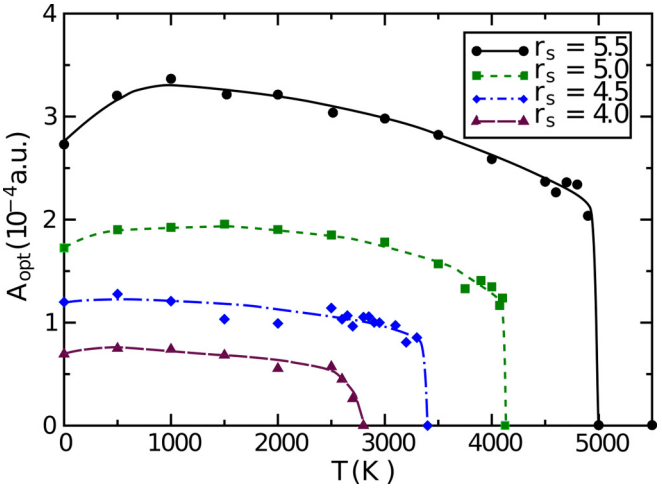

FIG. 7. Amplitudes A_{opt} of the equilibrium PSS phases as a function of T for various fixed $r_S = 4$, 4.5, 5, 5.5. The corresponding Fermi temperatures are $T_F = 36\,400$, 28 800, 23 300, 19 200 K.

TABLE III. Critical temperatures T_c^{PSS} above which no equilibrium PSS phase was found.

r_c	4.0	4.5	5.0	5.5
T_c(K)	2700	3400	4100	5000

(which corresponds to large r_S), the amplitude increases slightly when the temperature increases. This is somewhat surprising because the temperature is usually expected to favor states of higher disorder. Therefore, one would expect the amplitude to decrease. However, in our calculations we encounter the following behavior of the Fermi surface. For $q/k_F < 2$ the zero-temperature Fermi surface assumes an hourglasslike shape as depicted in Fig. 4. We find that increasing temperature smoothens the Fermi surface, which in turn leads to an increasing occupation around the "waist" of the hourglass. The angles $\Theta_{\mathbf{k}}$ are usually closer to $\pi/2$ for smaller values of k_z, which then leads to an increasing PSS amplitude A via Eq. (B10). In the following we discuss the numerical uncertainty of these findings. The energy differences for slightly changed momentum distributions are very small, but the amplitude shows a much stronger dependence. This also explains the big variance of the calculated optimal amplitudes, as shown in Fig. 7. However, we performed a careful minimization of the functional with several k-point mesh refinements and believe that our numerical findings are qualitatively correct. We argue that for small temperatures the amplitude of a PSS state increases. The optimal $\mathbf{q}$ vector, on the other hand, only slightly changes. Therefore, the optimal amplitude increases for small temperatures. An increasing amplitude of the PSS with increasing r_S at zero temperature has also been reported in Ref. [69]. Below a critical radius $r_c^{PSS} = 3.5$, we cannot resolve the amplitude of the PSS anymore. This reduction of the amplitude is mainly due to the fact that the energy difference between the PM and FM phases increases. Therefore, the optimal $\mathbf{q}$ approaches $2k_F$ (see Fig. 6). At finite temperatures, this leads to a decreasing critical temperature T_c^{PSS} with decreasing r_S, as shown in Table III. For those r_S, for which a polarized configuration is favorable over an unpolarized one, a formation of a PSS was found to increase the free energy.

Finally, we show the extended magnetic phase diagram of the HEG [beyond the collinear spin configuration as in Fig. 1(b)] in Fig. 8. Considering the collinear phases, the kinetic energy favors a PM configuration, whereas the exchange contribution is minimized for a FM one. At zero temperature, the different r_S dependencies lead to a magnetic phase transition at r_c. Including the entropy, which itself favors a PM phase, leads to a weakening and eventually vanishing FM phase with increasing temperature. The magnetic phase transition, between PM and FM phases for increasing r_S, was shown to be instantaneous while the transition from FM to PM phases for higher r_S is second order. As shown in Fig. 8, the continuous phase transitions occur close to the Fermi temperature T_F. The PSS phase shows a much stronger density dependence and is strongest for $4 \leqslant r_S \leqslant 6$. In this range we also notice a temperature-driven instantaneous phase transition between a PSS and PM phase. Qualitatively, this

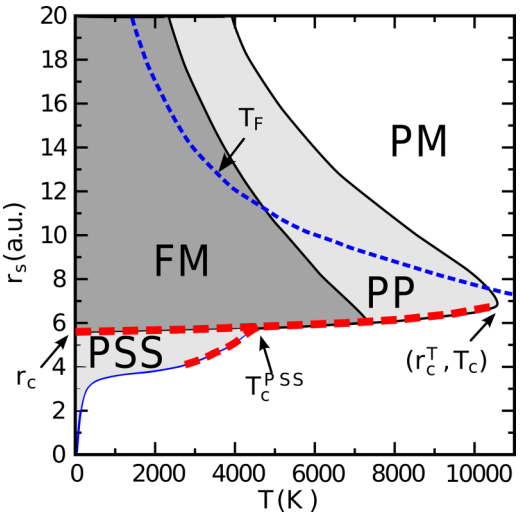

FIG. 8. Extended magnetic phase diagram of the HEG for the FT-RDMFT exchange functional. In addition to collinear spin configurations, it includes the PSS phase as an example of a noncollinear spin configuration. It predicts both instantaneous and continuous phase transitions for increasing r_S up to a critical temperature where the PM phase dominates. Note the unphysical, instantaneous phase transition both from the PM to the FM phase and from the PM to the PSS phase denoted by a dashed red line. The dashed blue line depicts the Fermi temperature T_F.

phase diagram agrees well with the phase diagram derived in Ref. [70], where a field-theoretical approach in combination with a contact-interaction approximation is employed. This method also yields a favorable PSS phase in the PM to FM phase transition at a fixed temperature, given that this temperature is below some critical value. This suggests that correlation functionals in FT-RDMFT should preserve this general property.

APPENDIX C: INSIGHTS FROM ZERO-TEMPERATURE RDMFT

1. Importance of the momentum distribution

The first requirement for an accurate FT-RDMFT functional is its ability to yield an accurate momentum distribution. The momentum distribution of the HEG in collinear spin configuration is known from highly accurate QMC calculations [55]. We condense these results into three main properties. The momentum distribution of the HEG displays the following:

(1) a nonzero occupation of all high momentum states [71] which can be understood through the electronic cusp condition [39,72];

(2) a discontinuity and symmetrical behavior around the Fermi level;

(3) a depletion of low-momentum states.

We evaluate existing functional approximations based on these criteria.

The simplest choice is to utilize density functional correlation approximations $\Omega_c[\gamma] = \Omega_c[\rho]$, i.e., functionals which just depend on the density ρ, rather than the 1RDM. However, this approach has an intrinsic flaw. In this case, we can write the minimization of the free energy as

$$F_{\mathrm{eq}} = \min_{\gamma} F[\gamma] = \min_{\rho} \min_{\gamma\to\rho} F[\gamma] \tag{C1}$$

$$= \min_{\rho}(V[\rho] + \Omega_H[\rho] + \Omega_c[\rho] + \min_{\gamma\to\rho}(\Omega_k[\gamma] - k_B T S_S[\gamma] + \Omega_x[\gamma])). \tag{C2}$$

Since $\Omega_C[\rho]$ is independent of the particular choice of 1RDM as long as these choices yield the same density, we can take it out of the minimization over 1RDMs. The remaining minimization over 1RDMs yields the Hartree-Fock momentum distribution which becomes a step function in the zero-temperature limit. Furthermore, this yields an *uncorrelated* 1RDM. Hence, utilizing $\Omega_C[\rho]$ completely fails in yielding the correct momentum distribution for low temperatures.

The situation is not better for RDMFT XC functionals. A brief discussion of existing functionals is given in Appendix A. None of these functionals yield momentum distributions that satisfy all exact properties (1)–(3). Property (1) is only recovered by the ML/ML-SIC functionals [65]. Property (2) is only recovered by the BBC [32] and PNOF [64] functionals partially. They yield momentum distributions with a discontinuity around the Fermi level, but these are not symmetric as required. Furthermore, they do not qualitatively resemble the QMC results. Additionally, the magnitude of the discontinuity created by the BBC functionals erroneously increases as r_S increases, whereas it should decrease [73]. Property (3) is fulfilled by none of these functionals.

We believe that the depletion of low-momentum states is an increasingly important physical effect in the low-density limit. It should, therefore, be recovered by an RDMFT XC functional. In the following, we derive the BOW and BOW-TIE functionals which incorporate this property.

2. Importance of spin-channel inseparability

The second requirement for an accurate FT-RDMFT XC functional is to be spin-channel inseparable. This requirement is related to the small energy differences between different magnetic phases in the HEG for low densities. A small error in the spin dependence of the XC functional might lead to large errors in the prediction of the critical density r_c. This sensitivity is even reflected in highly accurate QMC calculations. Despite their precision, their prediction for the critical density of the zero-temperature phase transition between the FM and PM phases spans a range from $r_c \approx 50$ [24] to $r_c \approx 75$ [46].

In RDMFT it is commonly assumed that the XC functional is spin-channel separable. Hence, the XC contributions from different spin channels are evaluated according to

$$E_{\mathrm{XC}}[\gamma] = E_{\mathrm{XC}}[\gamma_{\uparrow\uparrow},\gamma_{\downarrow\downarrow}] = E^S_{\mathrm{XC}}[\gamma_{\uparrow\uparrow}] + E^S_{\mathrm{XC}}[\gamma_{\downarrow\downarrow}], \tag{C3}$$

where $\gamma_{\uparrow\uparrow}$ and $\gamma_{\downarrow\downarrow}$ denote the diagonal elements of the 1RDM γ in spin space and $E^S_{\mathrm{XC}}[\gamma]$ the XC functional which just depends on one spin component of the 1RDM.

However, this separation into spin-channel contributions is only valid for the kinetic, external potential, and exchange energy components, whereas it is invalid for the correlation energy. We claim that an approximation to the correlation energy which assumes spin-channel separation is intrinsically incapable of accurately describing spin-polarized

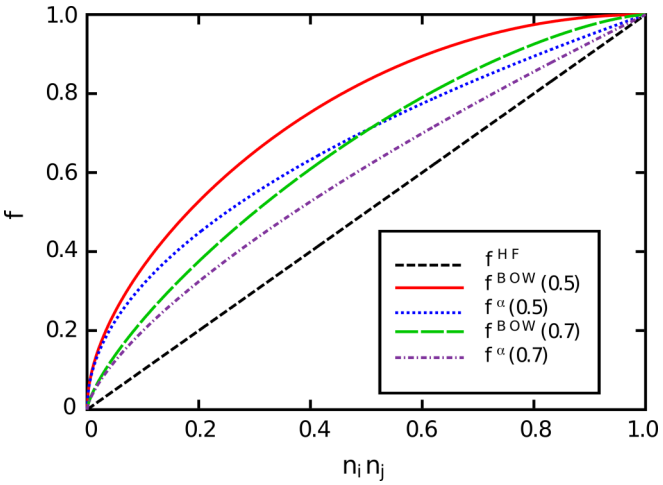

FIG. 9. Functional forms of the Hartree-Fock (f^{HF}), power (f^{α}), and BOW (f^{BOW}) functionals for different values of α. The Hartree-Fock functional is reproduced by both functionals with $\alpha = 1$.

and spin-unpolarized configurations. The underlying reason is that a separable functional as in Eq. (C3) might accurately capture the correlation contributions of same spin electrons, but will fail in capturing the correlation of opposite spin electrons. We demonstrate this for the HEG in Appendix D.

3. BOW functional at zero temperature

Our goal is to construct a zero-temperature RDMFT XC functional which (i) yields an accurate momentum distribution, i.e., both an occupation of high-momentum states as well as depletion of low-momentum states, and (ii) is spin-channel inseparable. The resulting zero-temperature RDMFT XC functional then serves as the basis for constructing FT-RDMFT XC functionals.

We propose the BOW functional

$$E_{\mathrm{XC}}^{\mathrm{BOW}}[\gamma;\alpha] = -\frac{1}{2}\sum_{ij\sigma} f^{\mathrm{BOW}}(n_{i\sigma},n_{j\sigma};\alpha)\int d\mathbf{r}\,d\mathbf{r}'\,w(\mathbf{r},\mathbf{r}')\phi_{i\sigma}^{*}$$
$$\times(\mathbf{r}')\phi_{i\sigma}(\mathbf{r})\phi_{j\sigma}^{*}(\mathbf{r})\phi_{j\sigma}(\mathbf{r}'), \tag{C4}$$

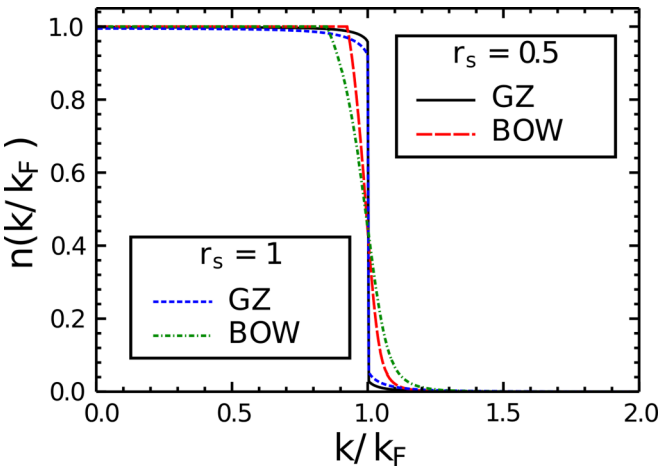

FIG. 10. Momentum distributions of the 3D HEG for $r_{\mathrm{S}} = 0.5$ and 1 obtained from the parametrization by Gori-Giorgi and Ziesche [55] and from the BOW functional for $\alpha = 0.61$.

TABLE IV. Optimal polarization-dependent parameter $\alpha(\xi)$ of the power and BOW functionals for the 3D HEG in the range $1 < r_{\mathrm{S}} < 100$.

ξ	Power functional $\alpha(\xi)$	BOW $\alpha(\xi)$
0.0	0.56	0.61
0.1	0.56	0.61
0.2	0.56	0.61
0.3	0.57	0.62
0.4	0.57	0.62
0.5	0.57	0.63
0.6	0.58	0.63
0.7	0.59	0.64
0.8	0.61	0.65
0.9	0.63	0.67
1.0	0.66	0.69

where

$$f^{\mathrm{BOW}}(n_{i\sigma},n_{j\sigma};\alpha) = (n_{i\sigma}n_{j\sigma})^{\alpha} - \alpha n_{i\sigma}n_{j\sigma} + \alpha$$
$$-\alpha(1-n_{i\sigma}n_{j\sigma})^{1/\alpha} \tag{C5}$$

which has a functional form satisfying both requirements.

With this choice of $f^{\mathrm{BOW}}(n_{i\sigma},n_{j\sigma};\alpha)$, we achieve an occupation of high-momentum states by incorporating the power functional $(n_{i\sigma}n_{j\sigma})^{\alpha}$ [38]. Furthermore, we achieve a depletion of low-momentum states by requiring a vanishing derivative $\partial E_{\mathrm{XC}}^{\mathrm{BOW}}/\partial n_{i\sigma}$ for $n_{i\sigma} = n_{j\sigma} = 1$ which is fulfilled by the functional form of $f^{\mathrm{BOW}}(n_{i\sigma},n_{j\sigma};\alpha)$. This allows to reduce the occupation of fully occupied states without changing the energy. To balance the weight of partially occupied states, we introduce the inverse of the power functional as a counterterm. The BOW functional reduces to the exchange-only functional for uncorrelated momentum distributions

$$f^{\mathrm{BOW}}(n_{i\sigma},n_{j\sigma};\alpha)|_{n_{i\sigma}n_{j\sigma}=0} = 0, \tag{C6}$$

$$f^{\mathrm{BOW}}(n_{i\sigma},n_{j\sigma};\alpha)|_{n_{i\sigma}=n_{i\sigma}=1} = 1. \tag{C7}$$

Furthermore, it reduces to the exchange-only functional when we choose $\alpha = 1$, i.e., $f^{\mathrm{BOW}}(n_{i\sigma},n_{j\sigma};1) = f^{x}(n_{i\sigma},n_{j\sigma})$.

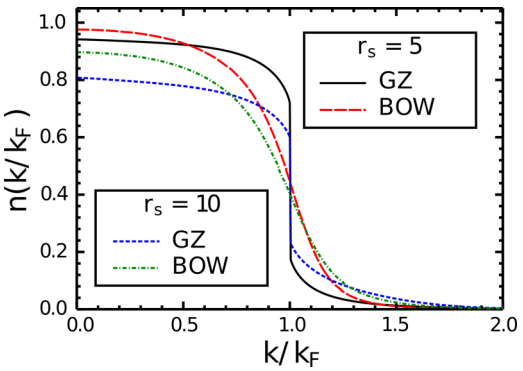

FIG. 11. Momentum distributions of the 3D HEG for $r_{\mathrm{S}} = 5$ and 10 obtained from the parametrization by Gori-Giorgi and Ziesche [55] and from the BOW functional for $\alpha = 0.61$.

TABLE V. Optimal parameters of the BOW-TIE functional defined in Eq. (C8).

	α^P	α^U	c
BOW-TIE	0.70	2.0	0.19

In analogy to the power functional, we control the influence of correlation in the BOW functional by tuning the parameter α. We compare the functional forms $f^{\mathrm{BOW}}(n_{i\sigma},n_{j\sigma};\alpha)$ and $f^{\alpha}(n_{i\sigma},n_{j\sigma};\alpha)=(n_{i\sigma}n_{j\sigma})^{\alpha}$ for various values of α in Fig. 9. Decreasing α leads to a bowlike shape of f^{BOW}, hence the choice of name.

The BOW functional yields an accurate momentum distribution. In Figs. 10 and 11 we assess its accuracy in comparison to the exact momentum distribution obtained from QMC calculations [55] for various Wigner-Seitz radii $r_S = 0.5$, 1.0, and 5.0. It yields both the occupation of high-momentum states and the depletion of low-momentum states accurately.

Unlike most of the existing RDMFT XC functionals (Müller, BBC1/2/3, PNOF/0, ML, ML-SIC), the BOW functional (as well as the power functional) is spin-channel inseparable. This is achieved by making α polarization dependent. The optimal $\alpha(\xi)$ for the power and the BOW functionals is given in Table IV.

Finally, we assess the accuracy of the BOW functional (with $\alpha = 0.61$) and other RDMFT XC functionals for the HEG in Fig. 12. As demonstrated, the BOW functional is remarkably accurate over a wide range of densities ($0.1 < r_S < 100$) including the range of metallic densities ($1 < r_S < 6$).

Despite its accuracy, the BOW functional fails to predict the magnetic quantum phase transition between the FM and the PM phases at zero temperature. For large r_S, where the phase transition should occur, it still favors the PM phase.

4. BOW-TIE functional at zero temperature

Next, we introduce a phenomenological correction to the BOW functional and recover the magnetic phase transition at zero temperature. Note that the BOW functional agrees well with QMC results for fully polarized spin configurations. We, therefore, propose to include the unploarized spin-channel contributions, i.e., the TIE in a similar way through a modification of the exchange integral. The final functional form of the resulting BOW-TIE functional reads as

$$E_{\mathrm{XC}}^{\text{BOW-TIE}}[\gamma] = -\frac{1}{2}\sum_{ij\sigma} f^{\mathrm{BOW}}(n_{i\sigma},n_{j\sigma};\alpha^P)K(i,j) - c\sum_{ij}((n_{i\uparrow}n_{j\downarrow})^{\alpha^U}(1-n_{i\uparrow}n_{j\downarrow})^{\alpha^U})K(i,j), \tag{C8}$$

where $K(i,j)$ denotes the exchange integral and α^P the optimal parameter for the fully polarized HEG. The second term in Eq. (C8) vanishes for a fully spin-polarized configuration and contributes increasingly with decreasing polarization. The parameters α^U and c are fitted to reproduce the critical density r_c of the HEG known from QMC calculations, while maintaining an overall accuracy for different spin polarizations. The resulting parameters summarized in Table V lead to an instantaneous phase transition at a critical density of $r_c \approx 28$ at zero temperature.

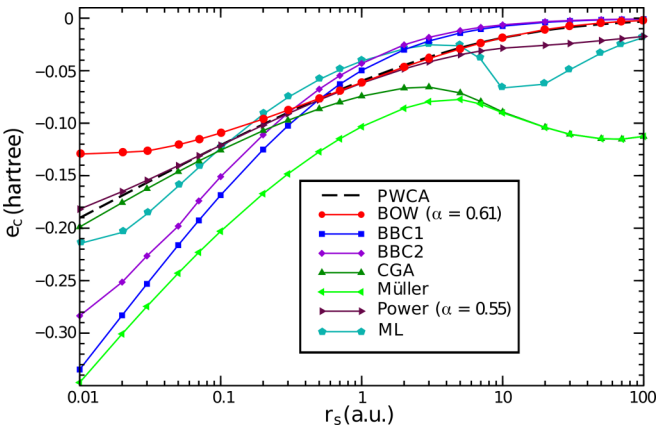

FIG. 12. Comparison of the exact QMC correlation energy of the 3D HEG in the PW parametrization [28] (black curve) with the predictions of the BOW functional (red curve) and various other RDMFT XC functionals.

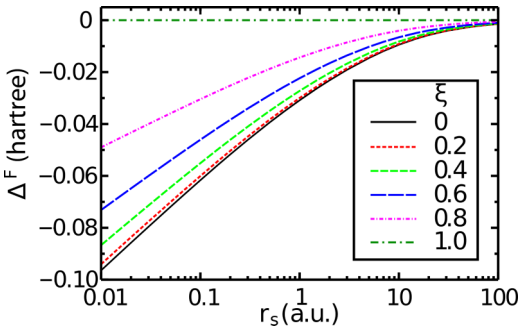

FIG. 13. Deviation Δ^P from QMC results for different polarizations $\xi \in [0,1]$.

APPENDIX D: FAILURE OF SPIN-CHANNEL SEPARABILITY

In this Appendix we demonstrate that the common approach of assuming spin-channel separable XC functionals in RDMFT as stated in Eq. (C3) fails in accurately describing

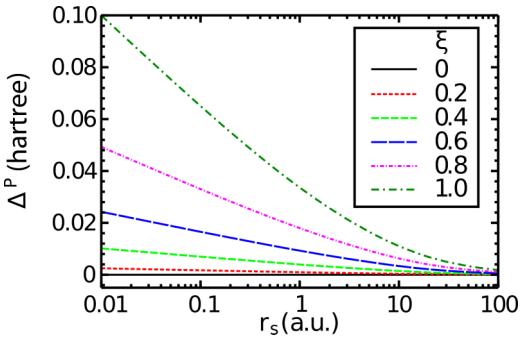

FIG. 14. Deviation Δ^P from QMC results for different polarizations $\xi \in [0,1]$.

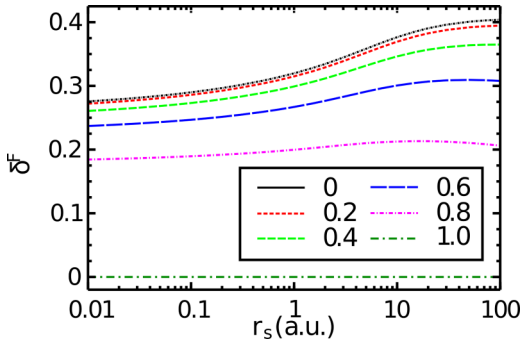

FIG. 15. Relative energy deviations δ^P from QMC results for different polarizations $\xi \in [0,1]$.

the PP spin configuration. Assuming spin-channel separability, we investigate the error introduced in the PP phase of the HEG based on the PW parametrization of QMC results. Consider a collinear spin configuration with the spin-up density $\rho_\uparrow$ and spin-down density $\rho_\downarrow$. Assuming spin-channel separability, we have two possibilities to calculate the total energy of a PP phase. We can either obtain it as a sum of two fully polarized systems

$$E^P_{\mathrm{PP}}(\rho_\uparrow,\rho_\downarrow) = E(\rho_\uparrow,0) + E(0,\rho_\downarrow) \tag{D1}$$

or as a sum of two unpolarized systems

$$E^U_{\mathrm{PP}}(\rho_\uparrow,\rho_\downarrow) = \tfrac{1}{2}[E(\rho_\uparrow,\rho_\uparrow) + E(\rho_\downarrow,\rho_\downarrow)]. \tag{D2}$$

We define the deviations of Eqs. (D1) and (D2) from the total energy of the PP phase E_{PP} obtained from QMC calculations as

$$\Delta^P = E_{\mathrm{PP}} - E^P_{\mathrm{PP}}, \tag{D3}$$

$$\Delta^U = E_{\mathrm{PP}} - E^U_{\mathrm{PP}}. \tag{D4}$$

We plot both Δ^P and Δ^U as a function of r_S for different values of the polarization $\xi \in [0,1]$ in Figs. 13 and 14.

By construction, Δ^P vanishes for a fully polarized configuration ($\xi = 1$). With decreasing polarization the deviation Δ^P increases in magnitude. Similarly, Δ^U vanishes by construction for the unpolarized configuration ($\xi = 0$). With increasing polarization, it then increases.

Recall that in RDMFT the correlation contribution does not contain any kinetic correlation. To further assess the

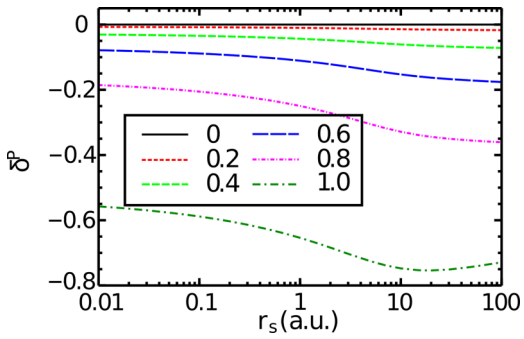

FIG. 16. Relative energy deviations δ^U from QMC results for different polarizations $\xi \in [0,1]$.

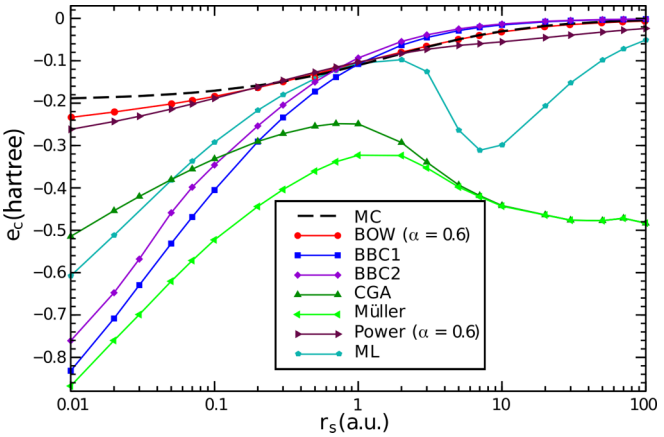

FIG. 17. Comparison of the exact QMC correlation energy of the 2D HEG in the Attaccalite parametrization [74] (black curve) with the predictions of the BOW functional (red curve) and various other RDMFT XC functionals.

error introduced due to assuming spin-channel separability, we define the two fractions

$$\delta^P = \frac{\Delta^P}{W_c}, \tag{D5}$$

$$\delta^U = \frac{\Delta^U}{W_c}, \tag{D6}$$

where $W_c = E_c - T_c$. The results are shown in Figs. 15 and 16. A remarkable feature is that the relative deviation over the whole range of considered densities does not vary strongly. Nevertheless, in conclusion we have shown that assuming spin-channel separability yields large errors for the correlation energy.

APPENDIX E: BOW FUNCTIONAL FOR THE 2D HEG

In this Appendix we assess the accuracy of the BOW functional for the 2D HEG. Its exact correlation energy

TABLE VI. Optimal polarization-dependent parameter $\alpha(\xi)$ of the power and BOW functionals for the 2D HEG in the range $1 < r_S < 100$.

ξ	Power functional $\alpha(\xi)$	BOW $\alpha(\xi)$
0.0	0.63	0.66
0.1	0.63	0.66
0.2	0.63	0.66
0.3	0.63	0.67
0.4	0.64	0.67
0.5	0.64	0.68
0.6	0.65	0.69
0.7	0.66	0.71
0.8	0.67	0.73
0.9	0.70	0.76
1.0	0.74	0.80

is known from accurate QMC calculations and has been parametrized [74].

First, we determine the optimal polarization-dependent parameter $\alpha(\xi)$ for the power and the BOW functionals. These are listed in Table VI.

Then, we calculate the correlation energy as a function of r_S with the BOW functional ($\alpha = 0.66$) and various other RDMFT XC functionals. We assess their accuracy in Fig. 17. Similarly as in 3D, the BOW functional is remarkably accurate over a wide range of densities.

[1] P. Hohenberg and W. Kohn, Phys. Rev. **136**, B864 (1964).
[2] W. Kohn and L. J. Sham, Phys. Rev. **140**, A1133 (1965).
[3] K. Burke, J. Chem. Phys. **136**, 150901 (2012).
[4] N. D. Mermin, Phys. Rev. **137**, A1441 (1965).
[5] *Frontiers and Challenges in Warm Dense Matter*, edited by F. Graziani, M. P. Desjarlais, R. Redmer, and S. B. Trickey, Lecture Notes in Computational Science and Engineering, Vol. 96 (Springer International, Switzerland, 2014).
[6] M. Levy, Proc. Natl. Acad. Sci. USA **76**, 6062 (1979).
[7] N. M. Rosengaard and B. Johansson, Phys. Rev. B **55**, 14975 (1997).
[8] G. Profeta, C. Franchini, N. N. Lathiotakis, A. Floris, A. Sanna, M. A. L. Marques, M. Lüders, S. Massidda, E. K. U. Gross, and A. Continenza, Phys. Rev. Lett. **96**, 047003 (2006).
[9] P. Cudazzo, G. Profeta, A. Sanna, A. Floris, A. Continenza, S. Massidda, and E. K. U. Gross, Phys. Rev. Lett. **100**, 257001 (2008).
[10] J. Gavnholt, A. Rubio, T. Olsen, K. S. Thygesen, and J. Schiøtz, Phys. Rev. B **79**, 195405 (2009).
[11] B. Militzer, Phys. Rev. Lett. **97**, 175501 (2006).
[12] S. Root, R. J. Magyar, J. H. Carpenter, D. L. Hanson, and T. R. Mattsson, Phys. Rev. Lett. **105**, 085501 (2010).
[13] M. W. C. Dharma-wardana and F. Perrot, Phys. Rev. A **26**, 2096 (1982).
[14] F. Perrot and M. W. C. Dharma-wardana, Phys. Rev. B **62**, 16536 (2000).
[15] M. W. C. Dharma-wardana and M. S. Murillo, Phys. Rev. E **77**, 026401 (2008).
[16] S. Atzeni and J. M.-T. Vehn, *The Physics of Inertial Fusion: Beam-Plasma Interaction, Hydrodynamics, Hot Dense Matter* (Clarendon Press, Oxford, 2004).
[17] M. D. Knudson and M. P. Desjarlais, Phys. Rev. Lett. **103**, 225501 (2009).
[18] W. Lorenzen, B. Holst, and R. Redmer, Phys. Rev. Lett. **102**, 115701 (2009).
[19] W. Lorenzen, B. Holst, and R. Redmer, Phys. Rev. B **84**, 235109 (2011).
[20] R. Redmer, T. R. Mattsson, N. Nettelmann, and M. French, Icarus **211**, 798 (2011).
[21] N. Nettelmann, A. Becker, B. Holst, and R. Redmer, Astrophys. J. **750**, 52 (2012).
[22] N. Nettelmann, R. Helled, J. Fortney, and R. Redmer, Planet. Space Sci. **77**, 143 (2013).
[23] G. Giuliani and G. Vignale, *Quantum Theory of the Electron Liquid*, Masters Series in Physics and Astronomy (Cambridge University Press, Cambridge, 2005).
[24] D. M. Ceperley and B. J. Alder, Phys. Rev. Lett. **45**, 566 (1980).
[25] D. M. Ceperley, Rev. Mod. Phys. **67**, 279 (1995).
[26] S. H. Vosko, L. Wilk, and M. Nusair, Can. J. Phys. **58**, 1200 (1980).
[27] J. P. Perdew and A. Zunger, Phys. Rev. B **23**, 5048 (1981).
[28] J. P. Perdew and Y. Wang, Phys. Rev. B **45**, 13244 (1992).
[29] E. W. Brown, B. K. Clark, J. L. DuBois, and D. M. Ceperley, Phys. Rev. Lett. **110**, 146405 (2013).
[30] E. W. Brown, J. L. DuBois, M. Holzmann, and D. M. Ceperley, Phys. Rev. B **88**, 081102 (2013).
[31] V. V. Karasiev, T. Sjostrom, J. Dufty, and S. B. Trickey, Phys. Rev. Lett. **112**, 076403 (2014).
[32] O. Gritsenko, K. Pernal, and E. J. Baerends, J. Chem. Phys. **122**, 204102 (2005).
[33] D. R. Rohr, K. Pernal, O. V. Gritsenko, and E. J. Baerends, J. Chem. Phys. **129**, 164105 (2008).
[34] N. N. Lathiotakis, S. Sharma, J. K. Dewhurst, F. G. Eich, M. A. L. Marques, and E. K. U. Gross, Phys. Rev. A **79**, 040501 (2009).
[35] D. R. Rohr, J. Toulouse, and K. Pernal, Phys. Rev. A **82**, 052502 (2010).
[36] N. Helbig, N. N. Lathiotakis, M. Albrecht, and E. K. U. Gross, Europhys. Lett. **77**, 67003 (2007).
[37] N. N. Lathiotakis, S. Sharma, N. Helbig, J. K. Dewhurst, M. A. L. Marques, F. G. Eich, T. Baldsiefen, A. Zacarias, and E. K. U. Gross, Z. Phys. Chem. **224**, 467 (2010).
[38] S. Sharma, J. K. Dewhurst, N. N. Lathiotakis, and E. K. U. Gross, Phys. Rev. B **78**, 201103 (2008).
[39] T. Baldsiefen, A. Cangi, and E. K. U. Gross, Phys. Rev. A **92**, 052514 (2015).
[40] T. Baldsiefen and E. Gross, Comput. Theor. Chem. **1003**, 114 (2013).
[41] P. Löwdin, Phys. Rev. **97**, 1474 (1955).
[42] A. Coleman, Rev. Mod. Phys. **35**, 668 (1963).
[43] J. E. Harriman, Phys. Rev. A **17**, 1257 (1978).
[44] D. Bohm and D. Pines, Phys. Rev. **92**, 609 (1953).
[45] J. Hubbard, Proc. R. Soc. London, Ser. A **243**, 336 (1958).
[46] F. H. Zong, C. Lin, and D. M. Ceperley, Phys. Rev. E **66**, 036703 (2002).
[47] G. G. Spink, R. J. Needs, and N. D. Drummond, Phys. Rev. B **88**, 085121 (2013).
[48] E. C. Stoner, Proc. R. Soc. London A **165**, 372 (1938).
[49] E. C. Stoner, Proc. R. Soc. London, Ser. A **169**, 339 (1939).
[50] S. Hong and G. D. Mahan, Phys. Rev. B **50**, 7284 (1994).
[51] S. Hong and G. D. Mahan, Phys. Rev. B **51**, 17417 (1995).
[52] S. Kurth, M. A. L. Marques, M. Lüders, and E. K. U. Gross, Phys. Rev. Lett. **83**, 2628 (1999).
[53] C. A. Ullrich and E. K. U. Gross, Aust. J. Phys. **49**, 103 (1996).
[54] K. Yasuda, Phys. Rev. Lett. **88**, 053001 (2002).
[55] P. Gori-Giorgi and P. Ziesche, Phys. Rev. B **66**, 235116 (2002).
[56] M. Troyer and U.-J. Wiese, Phys. Rev. Lett. **94**, 170201 (2005).
[57] M. K. Harbola, M. Hemanadhan, M. Shamim, and P. Samal, J. Phys.: Conf. Ser. **388**, 012011 (2012).
[58] U. Gupta and A. K. Rajagopal, Phys. Rev. A **22**, 2792 (1980).
[59] U. Gupta and A. Rajagopal, Phys. Rep. **87**, 259 (1982).
[60] S. Ismail-Beigi, Phys. Rev. B **81**, 195126 (2010).

[61] L. Hedin, Phys. Rev. **139**, A796 (1965).
[62] A. Müller, Phys. Lett. A **105**, 446 (1984).
[63] M. A. Buijse and E. Baerends, Mol. Phys. **100**, 401 (2002).
[64] M. Piris, J. M. Matxain, X. Lopez, and J. M. Ugalde, J. Chem. Phys. **132**, 031103 (2010).
[65] M. A. L. Marques and N. N. Lathiotakis, Phys. Rev. A **77**, 032509 (2008).
[66] N. N. Lathiotakis and M. A. L. Marques, J. Chem. Phys. **128**, 184103 (2008).
[67] P. W. Ayers, O. W. Day, and R. C. Morrison, Int. J. Quantum Chem. **69**, 541 (1998).
[68] A. W. Overhauser, Phys. Rev. **128**, 1437 (1962).
[69] F. G. Eich, S. Kurth, C. R. Proetto, S. Sharma, and E. K. U. Gross, Phys. Rev. B **81**, 024430 (2010).
[70] G. J. Conduit, A. G. Green, and B. D. Simons, Phys. Rev. Lett. **103**, 207201 (2009).
[71] J. C. Kimball, J. Phys. A: Math. Gen. **8**, 1513 (1975).
[72] G. Friesecke, Proc. R. Soc. London, Ser. A **459**, 47 (2003).
[73] N. N. Lathiotakis, N. Helbig, and E. K. U. Gross, Phys. Rev. B **75**, 195120 (2007).
[74] C. Attaccalite, S. Moroni, P. Gori-Giorgi, and G. B. Bachelet, Phys. Rev. Lett. **88**, 256601 (2002).